PHYSICAL REVIEW A **113**, 063111 (2026)

Universal approach to saddle-point methods in attosecond science

Anne Weber,[1,*] Job Feldbrugge,[2] and Emilio Pisanty[1]
[1]*Attosecond Quantum Physics Laboratory, Department of Physics,*
King's College London, Strand Campus, London WC2R 2LS, United Kingdom
[2]*Higgs Centre for Theoretical Physics, University of Edinburgh, Edinburgh EH8 9YL, United Kingdom*

(Received 22 October 2025; revised 30 March 2026; accepted 22 May 2026; published 22 June 2026)

Light-matter interactions within the strong-field regime, where intense laser fields can ionize a target via tunneling, give rise to fascinating phenomena such as the generation of high-order harmonic radiation (HHG) and, correspondingly, light pulses of attosecond duration. On the atomic scale, these strong-field processes are naturally described in terms of highly oscillatory time integrals which are often approximated using saddle-point methods. Those methods simultaneously simplify the calculations and let us understand the physical processes in terms of semiclassical electron trajectories, known as quantum orbits. However, applying saddle-point methods for HHG driven by polychromatic laser fields without clear dynamical symmetries has remained challenging. Here we introduce Picard–Lefschetz theory as a universal and robust link between the time integrals and the semiclassical trajectories, for arbitrary driving laser fields. The continuous deformation of the integration contour towards so-called Lefschetz thimbles allows for an exact evaluation of the integral, as well as the identification of relevant quantum orbits, independently of dynamical laser field symmetries or quantum-orbit classification heuristics. The latter is realized via the "necklace algorithm," a solution to the open problem of determining the relevance of saddle points for a two-dimensional integral, which we introduce here. We demonstrate the versatility and rigor of Picard–Lefschetz methods by studying Stokes transitions and spectral caustics arising in HHG driven by two-color laser fields. For example, we showcase a quantum-orbit analysis of the color switchover, which links the regime of perturbative two-color fields with that of fully bichromatic driving fields. With this work, we set the foundation for a rigorous application of quantum-orbit-based approaches in attosecond science that enables the interpretation of state-of-the-art experimental setups, and guides the design of future ones.

DOI: 10.1103/d2pt-xp7x

I. INTRODUCTION

In quantum mechanics, transitions between states can be described using Feynman's path-integral formalism, which considers all possible trajectories connecting initial and final states. Saddle-point methods (SPMs) allow this highly oscillatory integral to be approximated as a discrete sum over dominant, classical-like paths, providing both computational efficiency and physical insight. In attosecond science, a field with the goal of measuring atomic, electronic, and molecular dynamics on their natural timescale, SPMs have played a central role from the outset [1–3]. To probe the ultrafast dynamics, attosecond science relies on highly nonlinear light-matter effects such as above-threshold ionization (ATI) and high-order harmonic generation (HHG). The theoretical description of those optical processes within the strong-field approximation has been linked to a semiclassical picture of discrete electron trajectories dictated by monochromatic light fields, known as the *quantum-orbit formalism* [4–6]. However, the technological development of the past decades has enabled the use of more complex laser fields to drive the nonlinear optical processes. With that, the framework of SPMs has begun to show its limitations. Specifically, in the absence of temporal symmetries in the laser waveforms it becomes unclear which trajectories (i.e., which saddle points) contribute meaningfully to the dynamics.

Here, we introduce the methods of Picard–Lefschetz theory [7–10], the formalized generalization of all SPMs, as a universal approach to the most common integrals arising in attosecond science. Picard–Lefschetz theory suggests a rigorous mathematical definition of the Feynman path integral in terms of steepest-descent manifolds connected to saddle points of the phase function [11]. This allows the analysis of phenomena that were previously inaccessible to semiclassical methods like spectral caustics [12–17], and with that, provides a deeper understanding of the underlying quantum dynamics.

Within attosecond science, the strong-field approximation (SFA) is the main theoretical framework to describe the microscopic response of a gas atom subjected to a strong driving laser field whose peak intensity is comparable to the Coulomb force. The SFA offers an intuitive description of the process of HHG in terms of the three steps: (1) tunnel ionization, (2) propagation in the continuum and acceleration by the

---

[*] Contact author: anne.weber@kcl.ac.uk

driving field, and (3) recombination with the parent ion to emit a high-energetic photon [1,18,19]. The spectrum of high-energy photons typically covers a long range of frequencies (the HHG plateau), which temporally correspond to a train of short flashes of light—light pulses of attosecond duration. To understand and control the properties of this attosecond pulse it is necessary to understand the process of HHG for a range of different driving laser fields.

Nonsymmetric driving fields are of growing interest because they have demonstrated precise control over the temporal and polarization characteristics of the created HHG spectra [20–24] and offer additional insights to the quantum dynamics at play [25,26]. These tailored light fields are often a combination of laser fields of different frequencies and polarization. For example, a weak commensurate second color field can be used to modify strong-field ionization such that an additional phase delay scan allows to measure the intricate details of the tunneling process [27–30]. Going beyond the perturbative regime when adding a second field can extend the range of generated harmonic frequencies, increase the overall signal, and ultimately change the spectral and temporal properties of the created attosecond pulse [22,23,26,31–34]. Lastly, by creating three-dimensional polarization states of light it becomes possible to distinguish between chiral enantiomers of molecules [35,36]. The heuristics that were established to describe the atomic response in terms of discrete quantum orbits (corresponding to the different saddle points in the SPM), however, were developed for simple, monochromatic, and one-dimensional driving field shapes. They fail for those generic drivers with arbitrary waveform.

To overcome these limitations we need to advance our understanding of SPMs. Their mathematical backbone and the generalized approach to highly oscillatory and only conditionally convergent integrals is Picard–Lefschetz theory [7–9]. As such, Picard–Lefschetz theory has been introduced to solve high-dimensional path integrals in quantum field theories and was applied to solve path integrals in other areas of physics [10,37–41]. The fundamental idea is that there exists a continuous deformation (the downward flow) of the integration contour into the complex plane such that, evaluated along this new contour, the integrand oscillations minimize, while giving an exact formulation of the integral. This new contour is called the *Lefschetz thimble* and passes through the relevant saddle points of the integrand's phase function. Vice versa, this means that we can identify relevant saddle points by checking if the inverse deformation (i.e., the upward flow) lead back to the original integration contour.

The aim of this paper is to introduce Picard–Lefschetz theory to attosecond science. We demonstrate its effectiveness by addressing two challenges that remain inaccessible to the established semiclassical quantum-orbit methods: tackling configurations that exhibit caustics (where multiple saddle-point solutions coalesce) and, more generally, obtaining the strong-field response throughout any continuous parameter scan that changes the number of relevant trajectories. For that, this work is structured as follows. We begin in Sec. II with a brief overview of the existing quantum-orbit formalism for the ionization amplitude for strong-field tunneling and the dipole response for HHG, as examples of integrals over one and two dimensions, respectively. Section III introduces Picard–Lefschetz theory and, in particular, the two procedures for evaluating highly oscillatory integrals that we derive from it. The first is the numerical implementation of the continuous downward flow that deforms the integration contour into Lefschetz thimbles. The second is the "necklace algorithm", which we have developed to identify which of the critical points are relevant contributors in the saddle-point approximation of a two-dimensional integral.

These methods are then applied to strong-field physics in Sec. IV, where we consider HHG from two-color driving fields as an example. We present the harmonic response for driving-field configurations that produce swallowtail caustics over a two-color intensity ratio and phase-delay scan. Moreover, we use the saddle-point-based approach for the analysis of relevant electron trajectories in a setup where we gradually replace a monochromatic driver with its second harmonic, a technique termed color switchover [42], to demonstrate the versatility of our methods. Our open-source implementation of the numerical Picard–Lefschetz methods we develop and present here is available for use at [43], with the wrappers for calculating the strong-field ionization amplitude [44] and the HHG integral [45]. The specific implementation for this paper is deposited in Ref. [46].

II. QUANTUM-ORBIT APPROACHES IN STRONG-FIELD THEORY

The response of an atom to illumination by a laser pulse whose peak intensity is comparable with the strength of the binding Coulomb forces between nucleus and electrons can be described using the so-called strong-field approximation (SFA) framework [1,47–49]. The SFA consists of a set of approximations, most importantly assuming only one single active electron which is either in the ground state or in a Volkov-type continuum state where its motion is dictated entirely by the driving laser field and the drift momentum, neglecting the ion's Coulomb potential. Generally, these approximations can be extremely restrictive, but for laser peak intensities in the order of 10^{14} W/cm^2 and atomic gas targets, the SFA is indeed the preferred theoretical model, and in good agreement with experimental measurements [49]. Apart from numerical simplicity, the SFA also offers a quite intuitive understanding of the processes happening in these parameter ranges. Strong-field effects well described within the SFA include above-threshold ionization (ATI), nonsequential double ionization, high-harmonic generation (HHG), etc. [50].

In this paper, we focus on the two processes of direct ATI (via strong-field tunneling) and HHG. For both processes, the atomic response can be written as a Feynman path integral with the semiclassical action as an exponentiated phase function in the integrand [1,5,6]. That is, for ATI we consider the ionization probability and for HHG we consider the radiation dipole associated with the emitted photons. These types of integrals are highly oscillatory and can be solved using methods of stationary phase, also known as saddle-point methods [51,52]. By identifying stationary points of the exponent, i.e., saddle points of the action, the atomic response can be expressed in terms of Gaussian contributions from distinct ionization events (for ATI) and quantum orbits (for

HHG), in analogy to the least-action principle in Feynman's path-integral formalism.

However, in rewriting the continuous path integral to a sum over discrete contributions there are (at least) two intricacies that are often overlooked: First, the summation only runs over a strict subset of stationary solutions of the action. For example, all saddle-point solutions have their complex-conjugated counterpart which are typically ignored because the resulting contribution would be exponentially large and, hence, unphysical [48,53–55]. And second, in situations were saddle points are in close vicinity, their contribution is not actually of Gaussian shape. A prominent instance of this is the high-harmonic cutoff where the saddle-point solutions for the "short" and "long" trajectories perform a missed approach and their joint contributions are modeled in terms of an Airy function [54,56–58]. Both of these issues become particularly relevant when we start driving the processes not with simple one-dimensional monochromatic fields with dynamical symmetry, but instead with more complicated fields composed of multiple components of different polarizations, frequencies, etc. With every additional frequency component new saddle-point solutions arise. These potentially constitute new relevant quantum orbits, depending on the amplitude ratio and phase shifts between the constituent fields [59].

In the following we briefly describe the established procedures for the two considered processes of ATI and HHG and allude to how our current understanding of saddle-point methods is insufficient to describe state-of-the-art experimental setups.

A. Direct photoelectrons from above-threshold ionization in the strong-field tunneling regime

Electrons that tunnel through the barrier formed by the combination of Coulomb potential and the strong laser field's vector potential $\mathbf{A}(t)$ can be observed at a detector as direct photoelectrons. The spectrum of drift momenta $\mathbf{p}$ of those electrons is typically expressed in terms of the photoelectron ionization amplitude, given in atomic units as

$$\Psi(\mathbf{p}) = \int_{-\infty}^{\infty} P[\mathbf{p}+\mathbf{A}(t)]\mathrm{e}^{-\mathrm{i}S_{\mathrm{ATI}}(t)}\,\mathrm{d}t, \tag{1}$$

where the phase function

$$S_{\mathrm{ATI}}(t) = \int_{-\infty}^{t} \left[\mathcal{I}_{\mathrm{p}} + \frac{1}{2}[\mathbf{p}+\mathbf{A}(t')]^2\right]\mathrm{d}t' \tag{2}$$

is the semiclassical action of the electron, with the ionization potential $\mathcal{I}_{\mathrm{p}}$ [48]. The integration in Eq. (1) runs over the past time, and essentially includes the full interaction time with the laser field that drives the process. The prefactor $P(\mathbf{k})$ incorporates any information about the ground state of the atom and is assumed to depend smoothly on the canonical momentum $\mathbf{k} = \mathbf{p} + \mathbf{A}(t)$. Saddle points t_s of this semiclassical action are defined by

$$\left.\frac{\partial S_{\mathrm{ATI}}}{\partial t}\right|_{t=t_s} = \mathcal{I}_{\mathrm{p}} + \frac{1}{2}[\mathbf{p}+\mathbf{A}(t_s)]^2 = 0, \tag{3}$$

generally complex-valued for $\mathcal{I}_{\mathrm{p}} > 0$, and are interpreted as the discrete ionization times at which the electron escapes the Coulomb barrier [48]. The ionization amplitude (1) can then be rewritten as

$$\Psi(\mathbf{p}) \approx \sum_{t_s} \sqrt{\frac{2\pi}{\mathrm{i}S''_{\mathrm{ATI}}}}\,P[\mathbf{p}+\mathbf{A}(t_s)]\mathrm{e}^{-\mathrm{i}S_{\mathrm{ATI}}(t_s)}, \tag{4}$$

where the square-root term with the second derivative of the action comes in as we expand the exponential term around the saddle points t_s into a Gaussian shape and analytically integrate those, which is known as the standard saddle-point method [51,52].

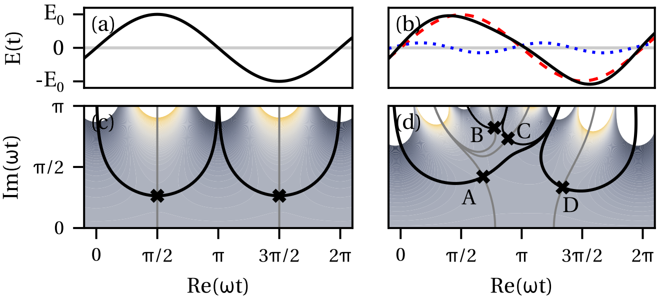

FIG. 1. Top row: (a) A simple monochromatic driving field, and (b) a two-color field composed of a ω field (red dashed) and a 2ω field (blue dotted) with phase shift $\varphi = 0.5$ and amplitude ratio $E_2/E_1 = 0.15$ according to Eq. (30). Bottom row: Contour plots of $\mathrm{Im}[S_{\mathrm{ATI}}(t)]$ (high values in yellow, low values in dark gray) for the complex t plane for the two driving fields shown on top, and drift momenta $p = p_x = 0$ and 1.2 a.u., respectively. Steepest-descent and steepest-ascent contour lines (black and gray lines, respectively) are attached to saddle points [black markers, labeled in (d) for convenience], with the resulting integration path drawn as a heavy black line.

Importantly, the sum in Eq. (4) only includes a subset of all the solutions to Eq. (3). To determine these *relevant* saddle points out of all solutions to Eq. (3), we need to identify a connected steepest-descent path that leads us in positive $\mathrm{Re}(t)$ direction, consistent with the original integration domain from $t = -\infty$ to ∞ in Eq. (1). For that, we allow our integration variable to take complex values, and plot the value of $\mathrm{Im}[S_{\mathrm{ATI}}(t)]$ across this complex plane of t, as this dictates the magnitude of the integral $|\mathrm{e}^{-\mathrm{i}S_{\mathrm{ATI}}(t)}| = \mathrm{e}^{\mathrm{Im}[S_{\mathrm{ATI}}(t)]}$. Because of the Cauchy-Riemann relations for complex analytic functions, the paths of steepest descent of $\mathrm{Im}[S_{\mathrm{ATI}}(t)]$ are then given by lines of constant $\mathrm{Re}[S_{\mathrm{ATI}}(t)]$.[1] A suitable integration path can therefore be found by plotting the contour level lines $\mathrm{Re}[S_{\mathrm{ATI}}(t)] = \mathrm{Re}[S_{\mathrm{ATI}}(t_s)]$ for each saddle point and then identifying a connected path.

For the simple monochromatic driving field $\mathbf{E}(t) = E_0\sin(\omega t)\mathbf{e}_x$ [shown in Fig. 1(a)] with $I_0 = E_0^2 = 0.92 \times 10^{14}\ \mathrm{W/cm^2}$ ($E_0 = 0.05$ a.u.), $\lambda = 1030$ nm ($\omega = 0.044$ a.u.), this is shown in Fig. 1(c), where we have used $\mathcal{I}_{\mathrm{p}} = 15.8$ eV, and $\mathbf{A}(t) = \int \mathbf{E}(t)\,\mathrm{d}t$. The corresponding contour plot of $\mathrm{Im}[S_{\mathrm{ATI}}(t)]$ is shown in Fig. 1(c), with high values ("hills") in yellow and low values ("valleys") in dark gray. In this action landscape we find two saddle points in the upper complex half-plane, at $\mathrm{Re}(\omega t) \approx \pi/2$ and $\approx 3\pi/2$ around the maxima of the field. Both are part of the connected

---

[1] See Sec. III A for the derivation.

steepest-descent integration path (heavy black line) and hence relevant contributors to the summation of ionization events in Eq. (4). This confirms the intuitive understanding of the process that at these times the distortion of the Coulomb potential is most significant and it is easiest for the electron to tunnel out.

In the case of a more complicated driving field, as shown in Fig. 1(b), the situation requires a bit more attention. Here there are four saddle points, which, for convenience, we have labeled A,B,C,D in the corresponding contour plot in Fig. 1(d). Drawing the respective contour level lines for each saddle point shows that a connected path in positive $\mathrm{Re}(t)$ direction can only be formed with the steepest-descent lines passing through points A and D, but not B and C. This lets us conclude that only A and D are contributors to the summation (4), whereas B and C need to be neglected.

While this approach of determining the relevance of specific saddle points seems intuitively promising, it is surprisingly nontrivial to develop an algorithm that finds connected steepest-descent contours in a robust and rigorous fashion [60,61]. Numerical instabilities are expected as soon as singularities enter the region of interest (viz., hills and valleys that are far away from the real axis) or when saddle points are in close vicinity. Furthermore, this approach still leaves us uninformed on how to solve the integral in the case of Stokes transitions (when steepest-descent contours connect directly between two saddle points) or coalescing saddles (resulting in more than two lines steeply descending from the higher-order saddle point).

Ultimately, even though we could technically decide over the relevance of saddle points on a case-by-case basis by examining the action landscapes, so far there is no robust method to determine the steepest-descent integration path. While the one-dimensional integration is at least heuristically understood, for the two-dimensional time integration there exists no meaningful strategy.

B. High-harmonic generation

The process of high-harmonic generation (HHG) from atomic gas targets is typically understood in terms of a three-step model: The electron escapes the atomic Coulomb potential via tunnel ionization (step 1), then propagates in the continuum where it is accelerated by the driving laser field (step 2), until it finally recombines with its parent ion. Upon recombination, a high-energy photon is emitted (step 3) whose frequency is a harmonic multiple of the fundamental driver's frequency ω [1,2,62,63]. The spectrum of the emitted radiation typically covers a long range of frequencies (the HHG plateau) followed by a sharp drop in intensity (the high-harmonic cutoff). The theoretical description that supports this intuitive picture is the above-mentioned SFA [1]. Starting from the time-dependent Schrödinger equation and incorporating this set of assumptions and approximations (find detailed explanations in, e.g., [49,64]) ultimately yields the so-called Lewenstein integral which describes the time-dependent dipole moment created at the final photoemission step. The measured quantity in an experiment is the spectral power or, rather, the spectral intensity for harmonic frequency $q\omega$,

$$I(q\omega) = (q\omega)^2 |\mathbf{D}(q\omega)|^2, \tag{5}$$

which uses the Fourier transform of the Lewenstein integral and $q \in \mathbb{R}$. The dipole moment $\mathbf{D}(q\omega)$ is given as the two-dimensional integral over ionization and recombination times t_i and t_r:

$$\begin{aligned}\mathbf{D}(q\omega) = \mathrm{i} \int_{-\infty}^{+\infty} \mathrm{d}t_\mathrm{r} \int_{-\infty}^{t_\mathrm{r}} \mathrm{d}t_\mathrm{i}\, &\mathbf{d}[\mathbf{p}_s(t_\mathrm{i}, t_\mathrm{r}) + \mathbf{A}(t_\mathrm{r})] \\ &\times \Upsilon[\mathbf{p}_s(t_\mathrm{i}, t_\mathrm{r}) + \mathbf{A}(t_\mathrm{i})] \\ &\times \left(\frac{2\pi}{\mathrm{i}(t_\mathrm{r} - t_\mathrm{i})}\right)^{3/2} \mathrm{e}^{-\mathrm{i}S_\mathrm{HHG}(t_\mathrm{i}, t_\mathrm{r})},\end{aligned} \tag{6}$$

with the semiclassical action

$$\begin{aligned}S_\mathrm{HHG}(t_\mathrm{i}, t_\mathrm{r}) = \frac{1}{2} \int_{t_\mathrm{i}}^{t_\mathrm{r}} &[\mathbf{p}_s(t_\mathrm{i}, t_\mathrm{r}) + \mathbf{A}(t)]^2\, \mathrm{d}t \\ &+ (t_\mathrm{r} - t_\mathrm{i})\mathcal{I}_\mathrm{p} - q\omega t_\mathrm{r}.\end{aligned} \tag{7}$$

The scalar factor $\Upsilon(\mathbf{k})$ denotes the transition dipole from the ground state into the excited state, while $\mathbf{d}(\mathbf{k})$ is the recombination matrix element [49] for the kinematic momentum $\mathbf{k}$. The stationary momentum associated with a given electron path between t_i and t_r is given by

$$\mathbf{p}_s(t_\mathrm{i}, t_\mathrm{r}) = -\frac{1}{t_\mathrm{r} - t_\mathrm{i}} \int_{t_\mathrm{i}}^{t_\mathrm{r}} \mathbf{A}(t)\, \mathrm{d}t \tag{8}$$

as a result of applying the saddle-point method to the integration over possible intermediate drift momenta $\mathbf{p}$.

Similar to the aforementioned one-dimensional time integral for ATI, the exponentiated action $S_\mathrm{HHG}(t_\mathrm{i}, t_\mathrm{r})$ makes the integral (6) highly oscillatory. Analogously, the integral can be understood as a sum of contributions from several quantum orbits, each associated with a stationary point $(t_{\mathrm{i},s}, t_{\mathrm{r},s})$ of the action S_HHG. The integral (6) is therefore often approximated as

$$\begin{aligned}\mathbf{D}(q\omega) \approx \sum_s \frac{2\pi}{\sqrt{-\det[S''_\mathrm{HHG}(t_{\mathrm{i},s}, t_{\mathrm{r},s})]}} &\mathbf{d}[\mathbf{p}_s(t_{\mathrm{i},s}, t_{\mathrm{r},s}) + \mathbf{A}(t_{\mathrm{r},s})] \\ &\times \Upsilon(\mathbf{p}_s(t_{\mathrm{i},s}, t_{\mathrm{r},s}) + \mathbf{A}(t_{\mathrm{i},s})) \\ &\times \left(\frac{2\pi}{\mathrm{i}(t_{\mathrm{r},s} - t_{\mathrm{i},s})}\right)^{3/2} \mathrm{e}^{-\mathrm{i}S_\mathrm{HHG}(t_{\mathrm{i},s}, t_{\mathrm{r},s})}.\end{aligned} \tag{9}$$

The stationary points are pairs of ionization and recombination time $(t_{\mathrm{i},s}, t_{\mathrm{r},s})$ for which the first derivatives vanish,

$$\frac{\partial S_\mathrm{HHG}}{\partial t_\mathrm{i}} = 0 \quad \text{and} \quad \frac{\partial S_\mathrm{HHG}}{\partial t_\mathrm{r}} = 0, \tag{10}$$

and are saddle points in the complex plane. Each of those saddle points $(t_{\mathrm{i},s}, t_{\mathrm{r},s})$ represents a semiclassical electron trajectory giving rise to the quantum-orbit formalism [4,65].

For a given harmonic order q there will be multiple solutions to Eq. (10), such that the total harmonic response typically consists of contributions from various interfering quantum orbits. Inspecting the ionization and recombination times for the different values of q, i.e., throughout the harmonic spectrum, traces "lines" in the complex planes for t_i and t_r, respectively; see Figs. 2(b) and 2(c) for the solutions

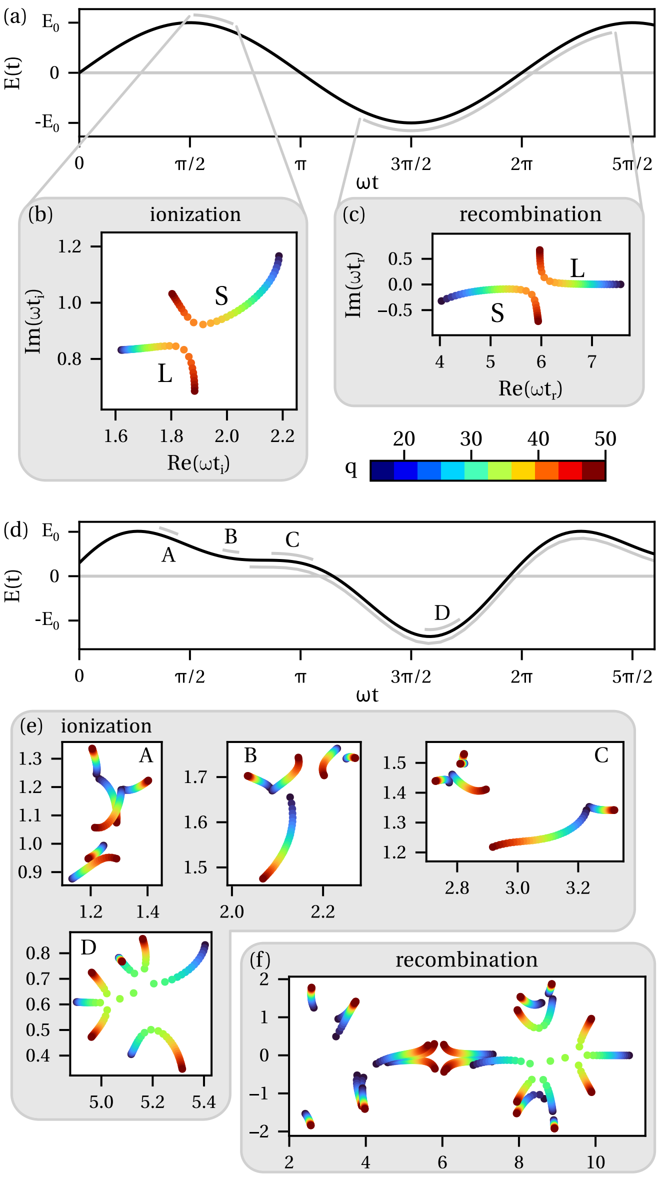

FIG. 2. Typical structure of the complex saddle-point solutions for HHG in the complex plane of ionization and recombination times. For the monochromatic driving field shown in (a) the solutions across a range of harmonic orders q (color bar) follow lines in the complex planes for ionization (b) and recombination (c) time, and can be classified as short (S) and long (L) trajectories. For the electric field shown in (d), a two-color field with $\varphi = 0.75$ and $E_2/E_1 = 0.44$, as per Eq. (30), the solutions still trace lines in the complex planes (e) and (f), and form several ionization windows [labelled A,B,C,D in (e)], but their structure is more intricate, hindering a classification.

around one ionization window of a monochromatic driving field shown in Fig. 2(a). Those lines make it easy to classify the various saddle-point solutions according to their travel time $\mathrm{Re}(t_{r,s} - t_{i,s})$ into "short" (S) and "long" (L) orbits, and associate them to the various ionization bursts within one cycle of the driving field [54,57,66].

As in the case of ATI, not all mathematical solutions to Eq. (10) are actually relevant quantum orbits. For example, we typically only consider those solutions where the ionization times have a positive imaginary part, $\mathrm{Im}(t_{i,s}) > 0$. Furthermore, for monochromatic driving fields, the short trajectories have to be discarded after the high-harmonic cutoff of the spectrum [57]. These heuristics, while often physically motivated, lack a consistent theoretical foundation and fail to generalize to arbitrary or continuously changing laser fields. They have been established without mathematical rigor and are often based on the fact that including other solutions leads to diverging integral values [53–55]. Moreover, the heuristics rely on the classification of the solutions.

For a generic driving laser field the structure of saddle-point ionization and recombination times in the complex plane may be much more complicated, as shown in Figs. 2(e) and 2(f) for the electric driving field in Fig. 2(d). In this particular case, we may attribute solutions to separate ionization windows (here labeled A–D) but a classification scheme for the individual solutions cannot easily be derived. Furthermore, the classification scheme breaks down once we consider smooth transitions of driving fields, for example, a scan through a phase delay between the two components of a two-color field [55]. In such cases, the saddle-point structures may change qualitatively, including coalescences and branch cuts. As a result, we are unable to determine relevant saddle points and therewith the contributing quantum orbits. This underscores the need for a more robust and systematic approach to applying saddle-point methods to the integral (6) for the case of arbitrary driving fields. Without such an approach, our ability to interpret strong-field phenomena in terms of quantum orbits remains fundamentally limited. The following section introduces Picard–Lefschetz theory as the rigorous framework to address these issues, in a generic form.

III. PICARD-LEFSCHETZ THEORY

Integrals of the form

$$I = \int_{\mathcal{C}_0 \subset \mathbb{R}^N} \mathrm{e}^{\mathrm{i}\phi(\mathbf{x})/\hbar}\, \mathrm{d}\mathbf{x}, \tag{11}$$

evaluated along a path $\mathcal{C}_0$ in real space with the real-valued phase function $\phi(\mathbf{x})$ are highly oscillatory and only conditionally convergent. This makes them notoriously difficult to evaluate numerically, especially in the semiclassical limit $\hbar \to 0$ (see Fig. 3 for an example). These types of path integrals appear across a vast range of research areas and each research area has developed different methods to solve them. As such, Picard–Lefschetz theory [7–9,67] was applied in physics in the context of Chern-Simons quantum field theory where it aids to solve the QCD sign problem [10]. After that, it was used in quantum cosmology to solve the conformal-factor problem [37,68], developed into a numerical technique for lensing problems in radio astronomy [40,69,70] and combined with Hamiltonian Monte Carlo techniques in an attempt to solve the sign problem in lattice field theory [71–73]. Most recently, it was used to develop a rigorous definition and evaluation technique of the real-time path integral [11,41,74,75]. We here give a very brief overview of the main ideas, illustrated by a one-dimensional example, before we lay out further details on the mathematical background, the numerical implementations, and the application to caustics and

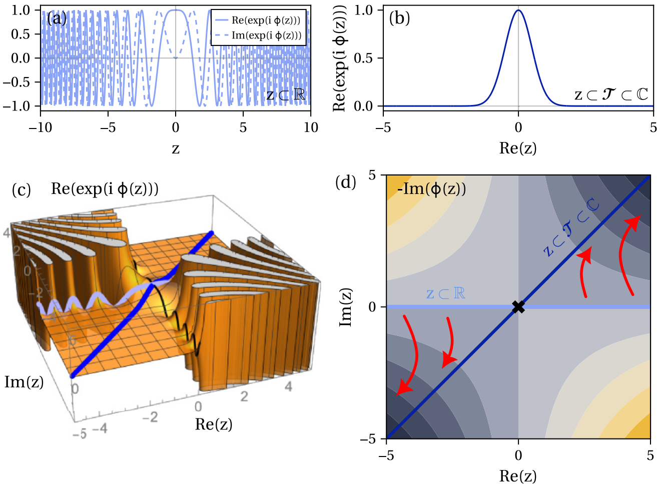

FIG. 3. Fundamental idea of Picard–Lefschetz theory, shown on the toy model function $\phi(z) = z^2$. The integrand e^{iz^2} is highly oscillatory when evaluated along the real axis (a). The continuation of z into the complex plane (c) shows that the oscillations (along the light blue line) vanish if we evaluate the integrand along a different contour (dark blue line). The contour that localizes the integrand by minimizing the oscillations follows steepest-descent paths of $\mathrm{Im}(z^2)$ [dark blue line in (d)] and is identified by deforming the original integration domain according to the downward flow (red arrows) and leads across the saddle point at $z = 0 + 0\mathrm{i}$, where $\phi'(z) = 0$. Often, the integrand along the new contour has Gaussian shape [as in (b)] and can be calculated analytically.

catastrophe theory, in the subsequent sections.[2] Further explanations can be found in Ref. [76]. The fundamental insight of Picard–Lefschetz theory, shown on a toy model function in Fig. 3, is to apply Cauchy's integral theorem and deform the integration contour $\mathcal{C} \subset \mathbb{R}^N$ into the complex space $\mathbb{C}^N$ such that along this new contour the integrand no longer oscillates, the integral converges absolutely, and hence is easier (if not trivial) to evaluate. Of course, the key question is: How do we find this optimal integration contour?

Assuming that $\phi(\mathbf{z})$ is a locally analytic function[3] of $\mathbf{z} \in \mathbb{C}^N$ we continuously deform the integration domain toward contours along which the amplitude of the integrand $|e^{i\phi}| = e^{\mathrm{Re}(i\phi)}$ decreases as rapidly as possible. The direction of the deformation is therefore given by the *downward flow*

$$\frac{\mathrm{d}\mathbf{z}}{\mathrm{d}\lambda} = -\left(\frac{\partial i\phi}{\partial \mathbf{z}}\right)^* \tag{12}$$

as a function of the real-valued flow parameter λ. "Flowing" a point $\mathbf{z} \in \mathbb{C}^N$ into the direction $-(\partial i\phi/\partial\mathbf{z})^*$ naturally moves it into the complex domain and toward the regions of lowest values of $i\phi$. Thanks to Cauchy's integral theorem, the integral remains preserved throughout this deformation while the properties of the integrand are improved. The resulting integration domain is the contour

$$\mathcal{T}(\lambda) = \{\mathbf{z}(\lambda, \mathbf{z}_0)\,|\,\mathbf{z}(\lambda = 0, \mathbf{z}_0) = \mathbf{z}_0 \in \mathcal{C}_0\}, \tag{13}$$

where the flow is initialized along the original integration domain $\mathcal{C}_0 \subset \mathbb{R}^N$. In the limit $\lambda \to \infty$ the contour $\mathcal{T}(\lambda)$ converges to a set[4] of steepest-descent manifolds $\mathcal{T}_\sigma \subset \mathbb{C}^N$, so-called Lefschetz "thimbles":

$$\mathcal{T} = \lim_{\lambda\to\infty} \mathcal{T}(\lambda) = \sum_\sigma n_\sigma \mathcal{T}_\sigma. \tag{14}$$

Each thimble is attached to a critical point $\mathbf{z}_\sigma$ of the phase function, as these are stationary solutions to the downward flow equation (12) [38]. The critical points are given by $\phi'(\mathbf{z}_\sigma) = 0$ and are saddle points in the complex space.

Importantly, the deformed integration contour $\mathcal{T}$ only includes a subset of all critical points. This subset is specified by the intersection number $n_\sigma \in \mathbb{Z}$, which counts whether the steepest-*ascent* manifold $\mathcal{K}_\sigma$ attached to a critical point $\mathbf{z}_\sigma$ intersects the original integration domain $\mathcal{C}_0 \subset \mathbb{R}^N$. That is, when the thimble of the critical point $\mathbf{z}_\sigma$ is relevant to the integral, there exists a point on the original integration domain such that the flow eventually reaches it in the limit $\lambda \to \infty$. Intuitively, because the downward flow defines a continuous, and hence "unambiguous," contour transformation, we can reverse this procedure. Relevant critical points are therefore those which have the steepest-ascent manifold connecting back to the original integration domain.

Let us briefly show how this contour deformation works in practice, using the example of the ionization probability amplitude for strong-field tunnel ionization, Eq. (1), which is a 1D integration over time (see Sec. II A). The phase term of the integrand is $i\phi(t)/\hbar = -iS_{\mathrm{ATI}}(t)$,[5] and the original integration contour $\mathcal{C}_0$ is the real t axis.

The continuous deformation of the integration contour $\mathcal{T}(\lambda)$ according to the downward flow (12) (where the gradient on the right-hand side is now given by $-\frac{\partial iS_{\mathrm{ATI}}(t)}{\partial t}$) is shown in Fig. 4 for the same parameter configuration as in Fig. 1(d). We show discrete steps i of the iteration procedure, representing increasing values of the flow parameter λ from left to right. The bottom row shows contour plots of $\mathrm{Re}(-iS_{\mathrm{ATI}}) = \mathrm{Im}(S_{\mathrm{ATI}})$ with the integration contour drawn in dark blue and the integrand $\exp[-iS_{\mathrm{ATI}}(t)]$ evaluated along this contour is shown in the panels above. While the integrand is highly oscillatory along the original, real-valued integration contour [Fig. 4(a), iteration step $i = 0$], the very rapid oscillations disappear as soon as the contour is deformed even only slightly into the complex plane, i.e., after a few flow steps [Fig. 4(b), $i = 10$]. The flow ultimately converges [Fig. 4(d), $i = 70$] to yield the steepest-descent contours attached to saddle points (black lines attached to the black markers), confirming the integration route shown in Fig. 1(d).

---

[2] You may skip those subchapters for now and return back to them if/when necessary.

[3] That is, it is meromorphic, i.e., locally complex differentiable, such that it can be approximated by a Taylor series almost everywhere in the complex space. A remark on notation: We are using $\mathbf{z}$ instead of $\mathbf{x}$ to highlight the continuation into the complex space $\mathbb{C}^N$.

[4] We acknowledge that strictly speaking Eq. (14) should be a union rather than a sum. However, for consistency with the literature and the *summation* over integral contributions in Eq. (15) we use a sum here as well.

[5] Note the sign change for the exponentiated functions!

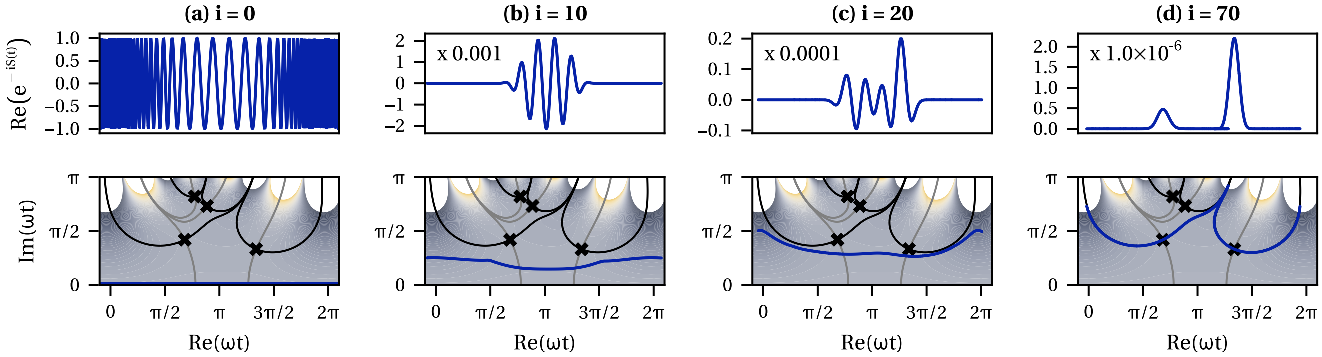

FIG. 4. Flowing the integration contour according to the downward flow, Eq. (12), for the same scenario as in Fig. 1(d) for discretized flow steps i (increasing left to right) to minimize the oscillations of the integrand. Bottom row: Action landscapes as in Fig. 1, with the integration contour highlighted in dark blue. Top row: The integrand of Eq. (1) evaluated along the respective contours.

Vice versa, the relevant saddle points are those which have a steepest-ascent contour connecting to the real axis and hence $n_\sigma = 1$. As $\mathrm{Im}(-\mathrm{i}S_{\mathrm{ATI}})$ is constant along the steepest-ascent contours, in this one-dimensional case these are simply the level lines at $\mathrm{Im}[-\mathrm{i}S_{\mathrm{ATI}}(t_s)]$. For the two saddle points with $\mathrm{Im}(\omega t_s) \approx 1.25$ [A and D from Fig. 1(d)] we find the level lines connect almost straight down to the real axis, whereas the steepest-ascent contours of the other two saddles (B and C, both around $2.5 + 2.5\mathrm{i}$) ultimately lead up into direction of higher imaginary parts, i.e., toward the hills of the contour plot, rendering $n_\sigma = 0$.

Upon the deformation of the contour according to the downward flow, the integral (11) can ultimately be expressed as a sum over contributions from the separate thimbles:[6]

$$I = \int_{\mathcal{C}\subset\mathbb{C}^N} \mathrm{e}^{\mathrm{i}\phi(\mathbf{z})/\hbar}\,\mathrm{d}\mathbf{z} = \sum_\sigma n_\sigma \int_{\mathcal{T}_\sigma\subset\mathbb{C}^N} \mathrm{e}^{\mathrm{i}\phi(\mathbf{z})/\hbar}\,\mathrm{d}\mathbf{z} \tag{15}$$

The value of the integral is thereby preserved at any intermediate stage λ of the downward flow. Notably, the expressions (11) and (15) are thus strict equalities, and independent of the dimension N, since all we have done so far is a contour deformation. However, for a nondegenerate critical point $\mathbf{z}_\sigma$ and in the asymptotic limit $\hbar \to 0$ the integral along its attached thimble can be approximated by a Gaussian [as in Fig. 3(c)]. This well-known approximation is the saddle-point method, as explained in, e.g., [51]:

$$\int_{\mathcal{T}_\sigma\subset\mathbb{C}^N} \mathrm{e}^{\mathrm{i}\phi(\mathbf{z})/\hbar}\,\mathrm{d}\mathbf{z} \approx \sqrt{\frac{2\pi\hbar}{\det(\phi''(\mathbf{z}_\sigma))}}\,\mathrm{e}^{\mathrm{i}\phi(\mathbf{z}_\sigma)/\hbar} \tag{16}$$

leading to the saddle-point approximation of the integral I,

$$I \approx \sum_\sigma n_\sigma \sqrt{\frac{2\pi\hbar}{\det[\phi''(\mathbf{z}_\sigma)]}}\,\mathrm{e}^{\mathrm{i}\phi(\mathbf{z}_\sigma)/\hbar}. \tag{17}$$

The saddle-point approximation inherits the relevance of the saddle point $\mathbf{z}_\sigma$ through the intersection n_σ.

On the example of the ionization amplitude, for the converged contour [Fig. 4(d)] we find the the contribution of each saddle point can be assumed Gaussian, such that the total value of the integral can be approximated by a sum of Gaussians around the two relevant t_s as shown in Eq. (4). Alternatively, we could terminate the flow procedure at any intermediate flow step i and integrate along the obtained contour in order to obtain the full integral.

With the reliable methods of evaluating an integral of type (11) by using either the downward flow of the integration contour or, alternatively, determining relevant saddle points via the intersection number, we can study the integral upon changes of external parameters of the phase function ϕ. In the case of strong-field physics, where the phase function is the semiclassical action of the electron in the continuum, those external parameters might be specifics of the driving laser field, for example, a phase shift in a two-color field configuration, or, in the case of HHG, the energy of the observed photon, i.e., the harmonic order.

Under a continuous variation of such external parameters, the saddle points $\vec{z}\sigma$ move smoothly in the complex $\mathbf{z}$ space, but may abruptly change their respective intersection number n_σ at Stokes transitions. Moreover, saddle points might coalesce into higher-order critical points, at which the conventional saddle-point approximation (16) breaks down because the second derivative ϕ'' in the denominator vanishes. To resolve the resulting caustics in the total integral we can use the downward flow, as it is in itself agnostic of the critical points. Evaluated across a range of external parameters it gives an exact representation of the integral regardless of possible "complications" in the saddle-point landscape.

In the following sections we will describe aspects of Picard–Lefschetz theory that are relevant to its application in attosecond physics. After giving a more detailed description of the inner working of the deformation of the integration contour in Sec. III A, we will present two possible approaches

---

[6] In this paper, we focus on the constructive interference of the integrand at the stationary points of exponent ϕ. However, in general, the sum of thimbles includes both steepest-descent manifolds associated with the stationary points of the exponent and the stationary points of the exponent restricted to the boundary of the original integration domain, i.e., $\phi|_{\mathcal{C}_0}$. These boundary thimbles are always relevant. However, the integral along the first set of thimbles typically dominates over the boundary thimbles. For a systematic investigation of the boundary points in Picard–Lefschetz theory, we refer to [77].

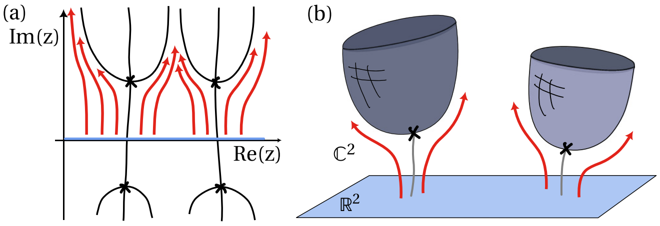

FIG. 5. For (a) one- and (b) two-dimensional path integrals the downward flow (directions indicated by red arrows) transform the original, real-valued integration domain (light blue) into the complex domain, ultimately toward the steepest-descent contours ("thimbles", gray) attached to the critical points (cross markers).

(and their numerical methods) to simplify the conditionally convergent highly oscillatory integral in Eq. (11): (a) *The downward flow*. Transforming the integration contour according to Eq. (12) and evaluating the integral along this new contour by numerical quadrature. (b) *The necklace algorithm*. Determining relevant critical points of $\phi(\mathbf{z})$ by checking if there exists a steepest-ascent connection to the original integration domain and then evaluating their integral on the thimble, or by their Gaussian approximation. Equipped with those robust techniques to evaluate whole families of integrals, in Sec. III C we will address the appearance of caustics in the space of external parameters.

A. On the deformation of the integration contour

Given that the exponent of the integrand in Eq. (11) is meromorphic it can be written as

$$\mathrm{i}\phi(\mathbf{z})/\hbar = h(\mathbf{z}) + \mathrm{i}H(\mathbf{z}), \tag{18}$$

where h controls the amplitude of the integrand as $|\mathrm{e}^{\mathrm{i}\phi}| = \mathrm{e}^{h}$, while H controls the oscillations.[7] That is, to localize the integrand we are seeking a contour along which the value of h decreases most rapidly and H is constant. As we analytically continue $\mathrm{i}\phi(\mathbf{z})$ into the complex plane, it fulfills the Cauchy-Riemann equations

$$\frac{\partial h}{\partial \mathrm{Re}(\mathbf{z})} = \frac{\partial H}{\partial \mathrm{Im}(\mathbf{z})} \quad \text{and} \quad \frac{\partial h}{\partial \mathrm{Im}(\mathbf{z})} = -\frac{\partial H}{\partial \mathrm{Re}(\mathbf{z})}. \tag{19}$$

Hence, contours of constant phase H are those along which e^{h} vanishes (or increases) most rapidly, making them contours of steepest descent (ascent). We can therefore find an optimal integration contour by deforming the integration path into the direction of decreasing h, using the downward flow, Eq. (12), shown above[8] and sketched in Fig. 5. Along the flow the value of H remains constant as

$$\frac{\partial \mathrm{i}\phi}{\partial \lambda} = \frac{\partial \mathrm{i}\phi}{\partial \mathbf{z}}\frac{\partial \mathbf{z}}{\partial \lambda} = \frac{\partial \mathrm{i}\phi}{\partial \mathbf{z}}\left(-\frac{\partial \mathrm{i}\phi}{\partial \mathbf{z}}\right)^{*} = -\left|\frac{\partial \mathrm{i}\phi}{\partial \mathbf{z}}\right|^{2} \tag{20}$$

which means that indeed $\mathrm{Im}\left(\frac{\partial \mathrm{i}\phi}{\partial \lambda}\right) = \frac{\partial H}{\partial \lambda} = 0$, while h decreases most rapidly: $\mathrm{Re}\left(\frac{\partial \mathrm{i}\phi}{\partial \lambda}\right) = \frac{\partial h}{\partial \lambda} < 0$. Flowing the entire original integration domain $\mathcal{C}_0$ into the complex plane converges the contour to a set of several disconnected Lefschetz thimbles [Eq. (14)]. Each thimble is a N-dimensional manifold embedded in $\mathbb{C}^N$ (i.e., $2N$ real dimensions) and attached to a critical point $\mathbf{z}_\sigma$, as mentioned above and visualized in Fig. 5 for $N = 1$ and 2 respectively. As $H(\mathbf{z}_\sigma)$ is constant along each of the thimbles $\mathcal{T}_\sigma \subset \mathbb{C}^N$, in the expression for the total integral (15) it acts as a weighing factor for each contribution. The integration only needs to be carried out across $\mathrm{e}^{h(\mathbf{z})}$:

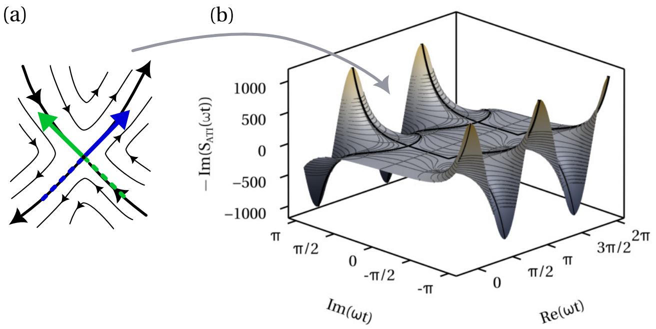

FIG. 6. For an analytical function zeros of the first derivative constitute saddle points in the complex plane, visible in the contour for $-\mathrm{Im}[S_{\mathrm{ATI}}(\omega t)]$ shown in (b). Around the saddle point ωt_s, level lines of $\mathrm{Im}[S_{\mathrm{ATI}}(\omega t)] = \mathrm{Im}[S_{\mathrm{ATI}}(\omega t_s)]$ (black) are locally orthogonal, as shown in (a), and define directions of steepest descent (blue) and steepest ascent (green) of $\mathrm{Re}[S_{\mathrm{ATI}}(\omega t)]$.

$$I = \sum_{\sigma} n_\sigma\, \mathrm{e}^{\mathrm{i}H(\mathbf{z}_\sigma)} \int_{\mathcal{T}_\sigma} \mathrm{e}^{h(\mathbf{z})}\, \mathrm{d}\mathbf{z}. \tag{21}$$

In analogy to the downward flow, the *upward flow* is given by

$$\frac{\mathrm{d}z_{\lambda,i}}{\mathrm{d}\lambda} = +\left(\frac{\partial \mathrm{i}\phi}{\partial z_{\lambda,i}}\right)^{*} \tag{22}$$

and shows the direction of steepest *ascent* of h, while preserving H. The steepest-ascent manifold of a saddle point $\mathbf{z}_\sigma$ is known as the *dual*[9] thimble $\mathcal{K}_\sigma \in \mathbb{C}^N$. The manifolds $\mathcal{T}_\sigma$ and $\mathcal{K}_\sigma$ intersect (and are locally orthogonal to each other) only in exactly one point: the critical point $\mathbf{z}_\sigma$, as it is a stationary solution to both upward and downward flow. This is visualized in Fig. 6(a) where steepest-descent (blue) and steepest-ascent (green) contours are locally orthogonal lines, intersecting at the saddle point. In the traditional treatment of saddle-point methods, the dual thimbles are often ignored. However, following Picard–Lefschetz theory, the dual thimble $\mathcal{K}_\sigma$ actually governs the relevance [meaning the contribution to the integral (15)] of the thimble $\mathcal{T}_\sigma$ through its intersections with the original integration domain $\mathcal{C}_0 \in \mathbb{R}^N$. Those intersections are counted by the intersection number

$$n_\sigma = \langle \mathcal{K}_\sigma, \mathcal{C}_0 \rangle, \quad n_\sigma \in \mathbb{Z}, \tag{23}$$

where the intersection operator $\langle \cdot, \cdot \rangle$ is rigorously defined in relative homology. If the dual thimble $\mathcal{K}_\sigma$ attached to a critical

---

[7] We use the notation $h = \mathrm{Re}(\phi)$ and $H = \mathrm{Im}(\phi)$ which is standard in the context of Picard–Lefschetz theory.

[8] Alternative names in other research areas are gradient, Morse, or holomorphic flow.

[9] Also referred to as the anti- or the unstable thimble [39,78].

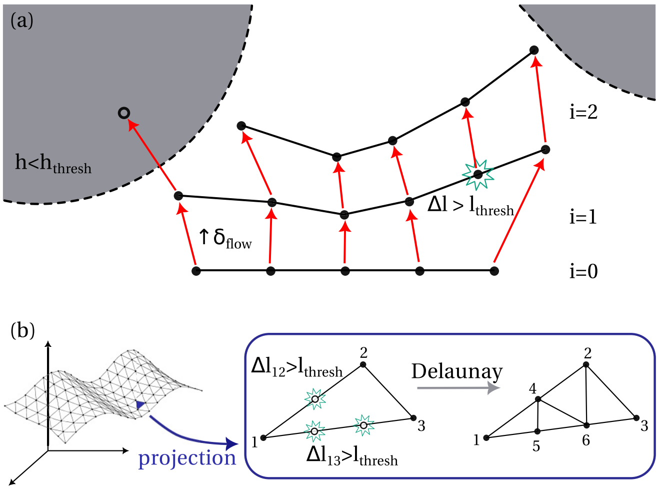

FIG. 7. Sketch of the implementation schemes of the downward flow procedure. (a) For a one-dimensional integration, the contour is discretized as a set of connected points that are iteratively (iteration step i) flowed in the direction given by the downward flow (red lines), possibly subdivided (newly inserted point on the right-hand side) and discarded (empty circle on the left-hand side). (b) The two-dimensional scheme follows the same procedure, but points are connected to triangles to form a surface. For the subdivision each triangle is considered in its projected plane, vertices are subdivided and the set of old and newly inserted points are connected to triangles by Delaunay triangulation.

point $\mathbf{z}_\sigma$ intersects the original integration domain ($n_\sigma \neq 0$), its thimble $\mathcal{T}_\sigma$ is part of the converged integration contour $\mathcal{T}$. If they do not intersect ($n_\sigma = 0$), the respective thimble has to be neglected.

B. Numerical methods for one- and two-dimensional integrals

The fact that the integration of a highly oscillatory, conditionally convergent integral can be localized into contributions from a discrete set of thimbles allows for a variety of computational approaches, e.g., finding the thimbles by means of Monte Carlo sampling when N is large [73,78,79]. In the following we describe the two methods that are well suited for the one- and two-dimensional integrals that describe strong-field ionization and HHG, respectively. First, the *downward flow*, which yields a discretized contour along which the integration can be carried out more efficiently. And secondy, the *necklace algorithm*, which we developed to determine the intersection number n_σ of a given saddle point, irrespective of any "classification" of saddle points (as one would usually do in attosecond science).

1. *The downward flow method*

The goal of the downward flow method is to deform the integration contour according to the downward flow (12). The numerical algorithm and its description are based on J.F.'s open-source implementation in C++, available at [80].

We will explain the algorithm for the case of a one-dimensional integral first, which is shown in Fig. 7(a). The initial step is the discretization of the (original) integration domain. We discretize the real axis as a list of points, which are connected to line segments. Then, we iteratively apply the downward flow to each of the points, moving it into the complex plane using a first-order Euler method

$$z \mapsto z - \delta_{\text{flow}} \left(\frac{\partial h}{\partial z}\right)^* \tag{24}$$

with the small parameter δ_{flow}. Note that it is sufficient to consider the gradient of h (rather than $i\phi$) as H remains constant along the flow anyway [see Eq. (20)]. We use an adaptive grid in the sense that as soon as two neighboring points are further than a threshold distance l_{thresh} apart, we insert a new point in the middle [see on the right-hand side in Fig. 7(a)]. Furthermore, points are turned "inactive" (such that they are not moved any more) as soon as their h value drops below a certain threshold, say h_{thresh}, indicated as gray regions and empty points in Fig. 7(a). This will eventually break up the integration contour into disconnected parts, as, e.g., in Fig. 4(d). The deformation of the integration contour converges to the Lefschetz thimble as $\frac{\partial h}{\partial z}$ vanishes on the thimble. To avoid "overshooting" this zero-gradient contour of steepest descent, we normalize the gradient as soon as its magnitude drops below a certain threshold. The algorithm is terminated after a fixed number of flow steps. This is necessary as the downward flow (24) itself continues to move points into the direction of steepest descent, viz., into the valleys. In other words, the flow of points never stops, but we find the resulting shape of the contour converges to resemble the steepest-descent contours. Conceptually, we may say the flow has converged when the number of active points remains constant (as points are replenished as shown in Fig. 7) and the shape of the contour does not change for subsequent iteration steps. In practice, however, a set maximum number of iteration steps proves more suitable.

In the case of a two-dimensional integral the algorithm technically follows the same procedure. However, each point now has two coordinates (each of them being a complex number!) and the integration "contour" is a surface, embedded in four real dimensions. That is, rather than using line segments we have discretized our integration domain into triangles now. For the subdivision we use the routine sketched in Fig. 7(b): each triangle is considered in its plane. For edges exceeding l_{thresh}, we insert $\lfloor \frac{\Delta l}{l_{\text{thresh}}} \rfloor$ new points and then mesh the original triangle using a Delaunay triangulation[10] of all points.

Ultimately, for the evaluation of the integral we use a numerical quadrature of the obtained meshed surface [81].

2. *The necklace algorithm*

Whether a given thimble $\mathcal{T}_\sigma$ contributes to Eq. (15) or not is dictated by the intersection number n_σ which counts the intersections between the dual thimble $\mathcal{K}_\sigma$ (the steepest-ascent manifold attached to a critical point) and the original integration domain $\mathcal{C}_0$. As the value of H is constant along the steepest-ascent manifold, for a one-dimensional integral ($N = 1$) finding the thimble and dual thimble attached to

---

[10] Coincidentally, the eponymous Boris Nikolayevich Delaunay is the father of Nikolai Borisovich Delone that gave the "D" in the Ammosov-Delone-Krainov (ADK) ionization rates in strong-field physics.

the critical point $z_\sigma \in \mathbb{C}$ corresponds to finding the respective contour level lines where $H(z) = H(z_\sigma)$, drawn as heavy black lines in Fig. 6, with arrows indicating the direction of descending h. This can easily be done numerically with, e.g., a marching squares algorithm. At the saddle point, these directions of maximized gradient are given by the (orthogonal) eigenvectors of the Hessian, one pointing in direction of steepest ascent (green), and one pointing in direction of steepest descent (blue). To find the dual thimble we therefore simply pick the contour level lines along which h increases away from the saddle point in the steepest-ascent direction. Locally, these lines coincide with the one of the eigenvectors and its inverse (dotted green vectors) of the Hessian. That is, if h is ascending along a level line away from z_σ and eventually connects to the real axis (the original integral domain), then $n_\sigma = 1$ and the critical point contributes to the integral. For example, in Fig. 6(a) for the saddle points with a positive imaginary part the steepest-ascent lines emanate in vertical direction from the saddle points and eventually intersect the real axis. For the saddle points with a negative imaginary part they emanate horizontally and do not reach the real axis. This can also be concluded immediately from the fact that for saddle points with $\mathrm{Im}(z_\sigma) < 0$ we have $h(z_\sigma) > 0$, such that there is no way "uphill" from z_σ to the real axis where $h = \mathrm{Re}\{\mathrm{i}\phi[\mathrm{Re}(z)]\} = 0$.

For the case of a two-dimensional integral, finding the dual thimbles is more complicated, as they are now two-dimensional manifolds (i.e., surfaces) embedded in the 4D space $[\mathrm{Re}(z_1), \mathrm{Im}(z_1), \mathrm{Re}(z_2), \mathrm{Im}(z_2)]$. That means, tracing the contour levels $H(\mathbf{z}) = H(\mathbf{z}_\sigma)$ for a critical point $\mathbf{z}_\sigma$ yields contour level *surfaces* embedded in four dimensions (4D), which is computationally more advanced.

Here we present a technique, which we call the "necklace algorithm", to determine the intersection number of a given saddle point for a two-dimensional integral, a problem which has so far remained open,[11] and for which tentative general solutions were only proposed very recently [84]. The basic idea, shown in Fig. 8, is to initialize the "tip" of the dual thimble in the closest vicinity of the saddle point, and then use the upward flow for its further construction "slice by slice." We terminate the upward flow as soon as each point reaches $h = 0$, and then check for the intersection with the original integration domain. As we are only interested in this (potential) intersection, it is sufficient to consider the "brim" of the thimble, which, as it is a discretized closed loop, we dub the necklace. This approach is guaranteed to identify *all* possible intersections of the steepest-ascent manifold with the original integration domain.

Let us briefly explain the procedure on the one-dimensional example. In the vicinity of the saddle point the direction of steepest descent and ascent can be found by linearizing the flow. That is, we calculate the second derivatives with respect to both real and imaginary parts of the integration variable z and identify the 2×2 real-valued Hessian matrix, the eigenvectors of which point in the direction of maximized gradient. The eigenvector corresponding to the negative eigenvalue points in direction of decreasing h away from the saddle point [drawn as a blue vector in Fig. 6(a)], whereas the eigenvector corresponding to the positive eigenvalue increases h away from the saddle point (drawn in green). To obtain the full steepest-ascent manifold (a line), we flow the end point of the steepest-ascent eigenvector and its inverse (drawn as a dashed vector in the opposite direction) until it eventually reaches $h = 0$.[12] If either of the end points of the line hits the real axis, the intersection number n_σ counts $+1$.

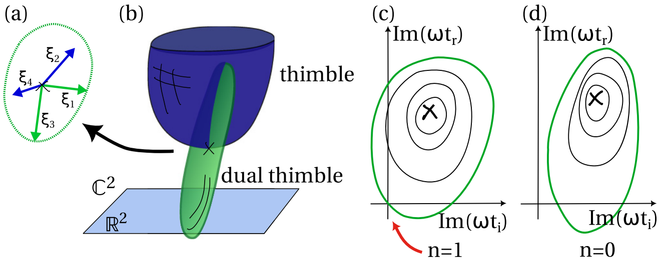

FIG. 8. The necklace algorithm: Thimble and dual thimble are surfaces embedded in 4D [illustrative 3D projection in (b)], locally spanned by the eigenvectors ξ_α of the Hessian at the saddle point (a). The brim of the dual thimble, the necklace, is initialized as a circle using the steepest-ascent eigenvectors (green), and then flowed upward. (c), (d) Projections of example necklaces in $[\mathrm{Im}(\omega t_\mathrm{i}), \mathrm{Im}(\omega t_\mathrm{r})]$, where an intersection with (0,0) implies an intersection with the real plane.

Now, for the two-dimensional integral we follow the same procedure. We assume that the upward flow (22) in a small region around the critical point $\mathbf{z}_\sigma$ is linear in h with respect to each of the four real-valued dimensions. That is, we use $\mathbf{z} = [\mathrm{Re}(z_1), \mathrm{Im}(z_1), \mathrm{Re}(z_2), \mathrm{Im}(z_2)]$ and write

$$\begin{aligned} \frac{dz_\alpha}{d\lambda} &= \left(\frac{\partial^2 h}{\partial z_\alpha \partial z_\beta} \right)^* \Bigg|_{\mathbf{z}=\mathbf{z}_\sigma} ({z_\beta}^* - {z_{\sigma,\beta}}^*) \\ &= \mathcal{H}_{\alpha\beta}({z_\beta}^* - {z_{\sigma,\beta}}^*), \end{aligned} \tag{25}$$

where $\alpha, \beta = 1 \ldots 4$, such that $\mathcal{H}$ is the real-valued, symmetric 4×4 Hessian of h. The solutions to the respective eigensystem

$$\mathcal{H}\tilde{\mathbf{v}} = \xi\tilde{\mathbf{v}} \tag{26}$$

yield four eigenvalues, coming in pairs, where $\xi_2 = -\xi_1$ and $\xi_4 = -\xi_3$. Analogously, for the corresponding eigenvectors we find $\tilde{\mathbf{v}}_2 = -\mathrm{i}\tilde{\mathbf{v}}_1$ and $\tilde{\mathbf{v}}_4 = -\mathrm{i}\tilde{\mathbf{v}}_3$. Their linear combination solves Eq. (25) and, hence, defines the directions of constant H around the saddle point $\mathbf{z}_\sigma$. The two vectors $\tilde{\mathbf{v}}$ with the smaller eigenvalues point toward the steepest descent of h, and the two vectors with larger eigenvalues point in the direction of steepest ascent of h, and they are drawn as blue and green vectors in Fig. 8(a), respectively. By rewriting the eigenvectors into complex form as $\mathbf{v}_\alpha = (\tilde{v}_{\alpha,1} + \mathrm{i}\tilde{v}_{\alpha,2}, \tilde{v}_{\alpha,3} + \mathrm{i}\tilde{v}_{\alpha,4})$, and assuming ξ_1 and ξ_3 to be the two positive eigenvalues,

---

[11] A similar approach has been used in [82,83] to approximate the (steepest-descent) thimbles.

[12] For the one-dimensional integral, of course, this is not usually necessary as we simply pick the respective contour level line.

we can therefore define the directions of steepest ascent,

$$\mathbf{z}(\lambda) - \mathbf{z}_\sigma = a_1 \mathbf{v}_1 e^{\xi_1 \lambda} + a_3 \mathbf{v}_3 e^{\xi_3 \lambda} \tag{27}$$

with arbitrary coefficients a_1 and a_3. We initialize the dual thimble's brim by constructing a vanishing cycle (viz., a "loop" of constant H) around the saddle point. For that we use the two steepest-ascent vectors and draw the circle

$$\mathbf{z}(\gamma, \lambda = 0) = \mathbf{z}_\sigma + \epsilon(\cos\gamma\, \mathbf{v_1} + \sin\gamma\, \mathbf{v_3}) \tag{28}$$

for $\gamma \in [0, 2\pi)$ and a small value ϵ, as shown in Fig. 8(a).

Once the necklace has been initialized, we discretize it and apply the upward flow (22) to each resulting bead of this necklace, making use of the procedure described for the downward flow in one dimension, and sketched in Fig. 7(a). With that we construct the dual thimble slice by slice (or rather, ring by ring) until all beads reach $h = 0$.

Finally, it remains indeed to check whether the found brim of the dual thimble intersects the original integration domain $\mathcal{C}_0$. For that we look at the $\mathrm{Im}(\mathbf{z})$ projection of the necklace and check if the line crosses the origin $\mathrm{Im}(\mathbf{z}) = (0, 0)$. This is shown schematically in Figs. 8(c) and 8(d), where in Fig. 8(c) we find the necklace intersects the real axis once, making $n_\sigma = 1$, whereas in Fig. 8(d) there is no intersection.

For any given individual saddle point, the necklace algorithm allows us to determine whether its thimble is a relevant contributor to the integral (15). As the necklace algorithm essentially traces contours of constant H value, limitations naturally arise in cases where two neighboring critical points have similar H values. The upward flow then might accidentally "slip" into (parts of) the dual thimble brim of the other critical point [76]. A decision about the relevance of the individual critical points can then be made by identifying the exact parameters for the Stokes transitions, as will be laid out in the next section.

Once we determined which saddle points constitute relevant thimbles, finding their contribution to the integral is straightforward. Either we apply the standard saddle-point method and approximate the integral across the thimble to be of Gaussian shape as shown in Eq. (16). Or, if we want an exact representation of the integral, we find the thimble attached to each critical point. For that, we initialize a small vanishing cycle around the critical point in the directions of steepest descent [by using the eigenvectors with smaller eigenvalues from Eq. (26)] and then construct the thimble by applying the *downward* flow to it slice by slice, analogously to flowing the necklace to obtain the dual thimble. The value of the integral can finally be found by evaluating the integrand along the thimble using a standard quadrature routine.

C. Evaluating integrals across ranges of external parameters: Stokes transitions, caustics, and catastrophes

Equipped with tools to solve integrals like Eq. (11) with arbitrary phase functions ϕ, we can study how they depend on external parameters. Upon a continuous scan over such external parameters, the saddle points $\mathbf{z}_\sigma$ vary smoothly in the complex $\mathbf{z}$ space. Their intersection number n_σ, however, may change abruptly at so-called *Stokes transitions*, causing the total number of contributing saddle points (or rather, thimbles) to change [54,56,57,85,86]. For this to happen there must be a topological change in the course of the steepest-descent integration contour. This is often caused by two (or more) critical points in close proximity, as shown in Fig. 9 for an integration contour depending on the external parameter q. In the left-hand panel where $q < q_{\mathrm{St}}$ the two critical points are both part of the converged deformed integration contour $\mathcal{T}$ (heavy blue line) and contribute separately to the integral via their thimbles $\mathcal{T}_{\sigma 1}$ and $\mathcal{T}_{\sigma 2}$. In the center panel, at $q = q_{\mathrm{St}}$, their steepest-descent contours coincide and the deformed contour contains both critical points. This value of the external parameter marks the Stokes transition. For a further increase of the external parameter where $q > q_{\mathrm{St}}$, the steepest-descent contours separate and $\mathcal{T}$ only contains one of the saddle points.

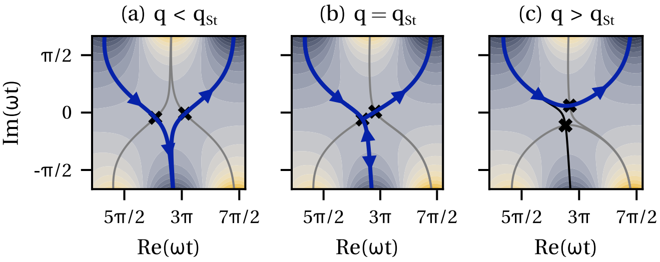

FIG. 9. Topological change of steepest-descent contours (black) and the resulting integration contour (heavy dark blue line) around a Stokes transition (at $q = q_{\mathrm{St}}$) between two saddle points upon changing an external parameter q (left to right panel).

A necessary condition for the Stokes transition between two critical points $\mathbf{z}_{\sigma 1}$ and $\mathbf{z}_{\sigma 2}$ is that $H(\mathbf{z}_{\sigma 1}) = H(\mathbf{z}_{\sigma 2})$, such that their steepest-descent contours may connect directly to each other. In simple examples, e.g., when $\phi(\mathbf{z})$ is a polynomial with two external parameters, Stokes transitions can be analytically solved for and yield lines in parameter space [40,87,88]. For more complicated $\phi(\mathbf{z})$, where there is no closed-form expression for $\mathbf{z}_\sigma$, candidate Stokes transition can be found numerically by identifying where in parameter space pairs of critical points assume the same value of H. Generally, for a phase function with K external "control" parameters the Stokes transitions are $(K-1)$-dimensional manifolds in the K-dimensional parameter space. They are topological features of this parameter space, as any change of number of relevant saddle points is indubitably linked to a Stokes transition. Vice versa, Stokes transitions define regions in parameter space with a certain number of contributors to the integral. Consequently, if they can be calculated *a priori* it is unnecessary to calculate each critical point's relevance individually.

More generally, as we evaluate the total integral across ranges of external parameters we find Stokes transitions and caustics. The latter are the pronounced features that arise whenever multiple saddle points are in close proximity and ultimately coalesce. Caustics can be observed in everyday life, e.g., the rippled bright features at the bottom of a swimming pool or the cusplike structure in a coffee cup, as well as in more involved physical problems like real-time path integrals, lensing (both optical and gravitational) [37,69], the formation of large-scale structures of our universe [89], and, of course, attosecond science [12–14,17]. From a mathematical point of view, caustics are best analyzed in terms of catastrophe theory. Assuming the phase function $\phi(\mathbf{z})$ is a $(K+2)$-order polynomial with K external control parameters, catastrophe theory dictates that there can be at most $K+1$ saddle points coalescing to one higher-order critical point: the catastrophe point. Evaluating the integral over a range of external parameters that involves such a coalescence of saddle points will yield characteristic patterns, depending on the codimension K, known as canonical diffraction patterns [90–92] (Sec. 36.3)]. Correspondingly, the contribution of a critical point in the vicinity of a coalescence cannot be taken as Gaussian, but has to be modeled using a uniform approximation that involves the canonical diffraction integrals, which is a challenging task [93–96]. For example, the diffraction pattern for the fold catastrophe ($K=1$), for which two saddle points coalesce, is the Airy function. Hence, the Airy function is used to model the HHG spectrum (which can be interpreted as a scan over the control parameter harmonic order) around the cutoff at which the saddle-point solutions for short and long trajectories (almost) coalesce [56,57].

The downward flow procedure elegantly circumvents these problems as it is agnostic to the critical points. With that, it offers the unique capability to evaluate the integral (11) exactly across parameter ranges and to naturally resolve the appearing caustic structures.

Having laid out the ideas and resulting numerical methods of Picard–Lefschetz theory, we now turn back to attosecond science and strong-field physics. In the following chapter we apply the methods introduced above to the SFA integral for HHG, namely, Eq. (6), and show how it allows for a quantum-orbit-based evaluation of scenarios with arbitrary driving waveforms.

IV. HHG DRIVEN BY TWO-COLOR LASER FIELDS

The harmonic response of an atom subjected to a strong laser field can (within the SFA framework [1,18]) be calculated in terms of the two-dimensional integral (6) over ionization and recombination times of the involved electronic wave packet, t_i and t_r, respectively. This double integral is often rewritten in terms of contributions of separate quantum orbits [6,65], which are the semiclassical electron paths defined by a discrete ionization and recombination time. This allows for an intuitive understanding of the process as the associated trajectories have different properties in the spatial divergences in the far-field [26,97]. The quantum orbits are pairs $(t_\mathrm{i}, t_\mathrm{r})$ for which the semiclassical action $S_\mathrm{HHG}(t_\mathrm{i}, t_\mathrm{r})$ is stationary, i.e., saddle points in the complex plane defined by Eq. (10). Notably, there are typically far more solutions to Eq. (10) than relevant quantum orbits to the process. So far, the existing heuristics to decide whether a given saddle-point solution is a relevant quantum orbit rely on a classification of the solutions and dynamic symmetries of the driving field.

For generic driving fields, however, those heuristics fail. In the following we demonstrate how the methods of Picard–Lefschetz theory described in Sec. III B can be utilized to compute the harmonic dipole integral (6). The central insight is that the integral can be evaluated along a different contour $\mathcal{C}$ in the complex time planes and ultimately expressed as a sum over contributions from separate thimbles $\mathcal{T}_s$:

$$\begin{aligned}\mathbf{D}(q\omega) &= \int_{\mathcal{C}_0} \dots \,\mathrm{d}\mathbf{t} = \int_{\mathcal{C}\in\mathbb{C}^2} \dots \,\mathrm{d}\mathbf{t}\\ &= \mathrm{i}\sum_s n_s \int\limits_{\mathcal{T}_s\in\mathbb{C}^2} \mathrm{d}\mathbf{t}\, \mathbf{d}[\mathbf{p}_s(t_\mathrm{i}, t_\mathrm{r}) + \mathbf{A}(t_\mathrm{r})]\\ &\quad \times \Upsilon[\mathbf{p}_s(t_\mathrm{i}, t_\mathrm{r}) + \mathbf{A}(t_\mathrm{i})]\\ &\quad \times \left(\frac{2\pi}{\mathrm{i}(t_\mathrm{r}-t_\mathrm{i})}\right)^{3/2} \mathrm{e}^{-\mathrm{i}S_\mathrm{HHG}(t_\mathrm{i}, t_\mathrm{r})}. \end{aligned} \tag{29}$$

Here, we notate $\mathbf{t} = (t_\mathrm{i}, t_\mathrm{r})$ and the original integration domain is $\mathcal{C}_0 = \{(t_\mathrm{i}, t_\mathrm{r}) \in \mathbb{R}^2 \mid t_\mathrm{r} > t_\mathrm{i}\}$. Each thimble $\mathcal{T}_s$ is attached to a critical point $(t_{\mathrm{i},s}, t_{\mathrm{r},s})$ defined by Eq. (10), and only contributes for nonvanishing intersection numbers n_s. The key difference to and striking advantage over Eq. (9) is that here we still have an equality, as we have not made any assumption on the shape of the integrand around the critical points.

Note that the presented integration methods “only” address the two-dimensional temporal integration and therefore hold for any definition of prefactors, waveforms, etc. With that, the exponentiated phase factor is $-\mathrm{i}S_\mathrm{HHG}$, which we consider in its dependency on ionization and recombination times only, $S_\mathrm{HHG} = S_\mathrm{HHG}(t_\mathrm{i}, t_\mathrm{r})$ as in Eq. (7).

As an example, within this paper we choose to consider HHG driven by a collinear and copolarized two-color field that consists of a fundamental laser field with frequency ω, superimposed with its second harmonic. A generic expression for the electric field then reads as

$$\mathbf{E}(t) = E_1 \cos(\omega t)\mathbf{e}_x + E_2 \cos(2\omega t + \varphi)\mathbf{e}_x \tag{30}$$

with the field amplitudes E_1 and E_2 and the phase delay φ between the two field components. For pulses longer than a few cycles, it is a good approximation to restrict our considerations to one cycle of the fundamental frequency, the period $T = 2\pi/\omega$. These types of driving fields are ubiquitous in attosecond science, in both experiment and theory. They allow to probe the inner workings of the process of strong-field light-matter interaction itself, as well as to tailor the properties of the harmonic spectrum and/or the created attosecond pulse [14,22,23,25,27,31,98]. The application of the described methods to two- or three-dimensional driving fields, as well as considering an entire pulse duration, is straightforward [76,99].

The following results are obtained using $\mathcal{I}_\mathrm{p} = 15.8\,\mathrm{eV}$ (argon) and $I_0 = E_0^2 = 0.92 \times 10^{14}\ \mathrm{W/cm^2}$ ($E_0 = 0.05$ a.u.), $\lambda = 1030\,\mathrm{nm}$ ($\omega = 0.044$ a.u.), and we use atomic units (a.u.) unless stated otherwise.

A. Applying Picard–Lefschetz methods

1. Using the downward flow to deform the integration contour towards Lefschetz thimbles

In the previous section we showed that there exists a continuous deformation of the original integration domain into a contour that minimises the integrand oscillations, which then allows for a more efficient numerical evaluation of the integrand along that new contour. We demonstrate how this

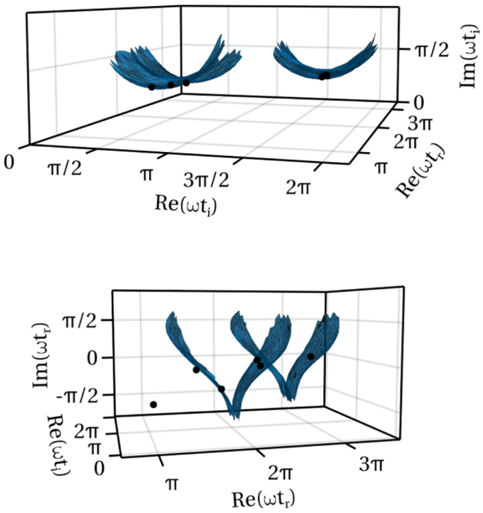

FIG. 10. Two projections of the HHG thimble for a monochromatic driving field and $q = 25$: Top: ionization-time projection $[\mathrm{Re}(t_\mathrm{i}), \mathrm{Im}(t_\mathrm{i}), \mathrm{Re}(t_\mathrm{r})]$ and Bottom: recombination-time projection $[\mathrm{Re}(t_\mathrm{r}), \mathrm{Im}(t_\mathrm{r}), \mathrm{Re}(t_\mathrm{i})]$. Saddle points are marked as black dots.

downward flow method is applied to the integration contour of the HHG integral Eq. (6).

We restrict ionization to one cycle, so $0 \leqslant \mathrm{Re}(t_\mathrm{i}) < T$, and recombination to happen after that, with travel times limited to one cycle as contributions from orbits with longer travel times are lower. This original integration domain is then deformed into the complex domain for both t_i and t_r, i.e., into the 4D space $[\mathrm{Re}(t_\mathrm{i}), \mathrm{Im}(t_\mathrm{i}), \mathrm{Re}(t_\mathrm{r}), \mathrm{Im}(t_\mathrm{r})]$. As described in Sec. III B, the deformation of the domain follows a simple first-order scheme for either variable,

$$t_\mathrm{i} \mapsto t_\mathrm{i} + \delta_\mathrm{flow} \frac{\mathrm{d}t_\mathrm{i}}{\mathrm{d}\lambda} \quad \text{and} \quad t_\mathrm{r} \mapsto t_\mathrm{r} + \delta_\mathrm{flow} \frac{\mathrm{d}t_\mathrm{r}}{\mathrm{d}\lambda}, \tag{31}$$

with a small factor δ_flow. The direction for every flow step λ is dictated by the downward flow Eq. (12), recast for the case of HHG:[13]

$$\frac{\mathrm{d}t_\mathrm{i}}{\mathrm{d}\lambda} = -\left(\frac{\partial S_\mathrm{HHG}}{\partial t_\mathrm{i}}\right)^* \quad \text{and} \quad \frac{\mathrm{d}t_\mathrm{r}}{\mathrm{d}\lambda} = -\left(\frac{\partial S_\mathrm{HHG}}{\partial t_\mathrm{r}}\right)^*. \tag{32}$$

This routine continuously deforms the (discretized) original integration domain into a two-dimensional steepest-descent surface embedded in 4D space and converges to the Lefschetz thimbles.

The resulting thimbles for the simple case of a monochromatic driver $E(t) = E_0 \cos(\omega t)$ [shown in Fig. 1(a)] and harmonic order $q = 25$ are shown in Fig. 10 in two projections, as well as the saddle-point solutions (black markers). In the "ionization-time projection" $[\mathrm{Re}(t_\mathrm{i}), \mathrm{Im}(t_\mathrm{i}), \mathrm{Re}(t_\mathrm{r})]$ (top), we observe the deformation into four disconnected surfaces corresponding to the ionization windows around each maximum of the electric field. In the "recombination-time projection" $[\mathrm{Re}(t_\mathrm{r}), \mathrm{Im}(t_\mathrm{r}), \mathrm{Re}(t_\mathrm{i})]$ (bottom), we identify four separate surfaces, corresponding to the expected two pairs of "short" and "long" quantum orbits within each half-cycle. Each surface is the steepest-descent manifold (thimble) of a relevant saddle point. Saddle points that are not included in the surface are irrelevant.

For comparison, and in order to aid the understanding of the flow method, we show a range of intermediate steps of the continuous deformation for a more complicated situation in Fig. 11. The driving field is the two-color field as in Fig. 1(b), and we show how the downward flow deforms the integration domain toward the Lefschetz thimbles (increasing iteration steps from left to right) for harmonic order 25, using the same projections as above. From the ionization-time projection (top row) we can make out separate ionization windows, albeit not as distinct as in the monochromatic case.

Finally, the harmonic dipole (6) can be calculated with a simple quadrature along these discretized Lefschetz thimbles. This can be done at any intermediate step of the deformation as the integral remains unchanged for just a change of contour [see Eq. (15)]. Note that this deformation of the integration domain is not an efficient method for the detection of all relevant saddle points.

2. Using the necklace algorithm to determine relevant quantum orbits

Saddle points of the action correspond to the quantum orbits that interfere when creating the harmonic dipole response. The properties of those several electron trajectories, e.g., the spread of the wave packet and the recollision angle, imprint on the dipole and therewith on the properties of the emitted radiation [27,28,100–103]. Moreover, the contributions of the various quantum paths behave differently upon propagation and give rise to distinct patterns in the far-field spectra measurement [33,104–106]. Phenomenologically, it is therefore interesting to understand which quantum orbits are at play for the creation of a certain dipole, i.e., to understand which saddle points are relevant contributors to the sum (29). A given saddle point is a relevant contributor if and only if its attached steepest-ascent contour (the dual thimble) connects back to the original integration domain. We find this possible intersection by propagating the brim of the dual thimble upward until $h = 0$ and then checking for an intersection of this brim with the real plane; this is the "necklace algorithm" introduced in Sec. III B 2. The necklace around the saddle point is initialized as a small circle in the plane of the two eigenvectors corresponding to the largest eigenvalues of the matrix

$$\mathcal{H}_{\alpha,\beta} = \frac{\partial^2}{\partial t_\alpha \partial t_\beta} S_\mathrm{HHG}(t_1 + t_2\mathrm{i}, t_3 + t_4\mathrm{i}), \tag{33}$$

where $\alpha, \beta = 1, \ldots, 4$, and where we have taken $\mathbf{t} = [\mathrm{Re}(t_\mathrm{i}), \mathrm{Im}(t_\mathrm{i}), \mathrm{Re}(t_\mathrm{r}), \mathrm{Im}(t_\mathrm{r})]$. Each bead of the (discretized) necklace then flows upward in h, following

$$\frac{\mathrm{d}t_\mathrm{i}}{\mathrm{d}\lambda} = +\left(\frac{\partial S_\mathrm{HHG}}{\partial t_\mathrm{i}}\right)^* \quad \text{and} \quad \frac{\mathrm{d}t_\mathrm{r}}{\mathrm{d}\lambda} = +\left(\frac{\partial S_\mathrm{HHG}}{\partial t_\mathrm{r}}\right)^* \tag{34}$$

until $h = 0$ and S_HHG becomes real. If the converged necklace intersects the original integration domain, the given saddle point is relevant. If not, then it is not relevant.

---

[13] We have dropped the λ indices for better readability.

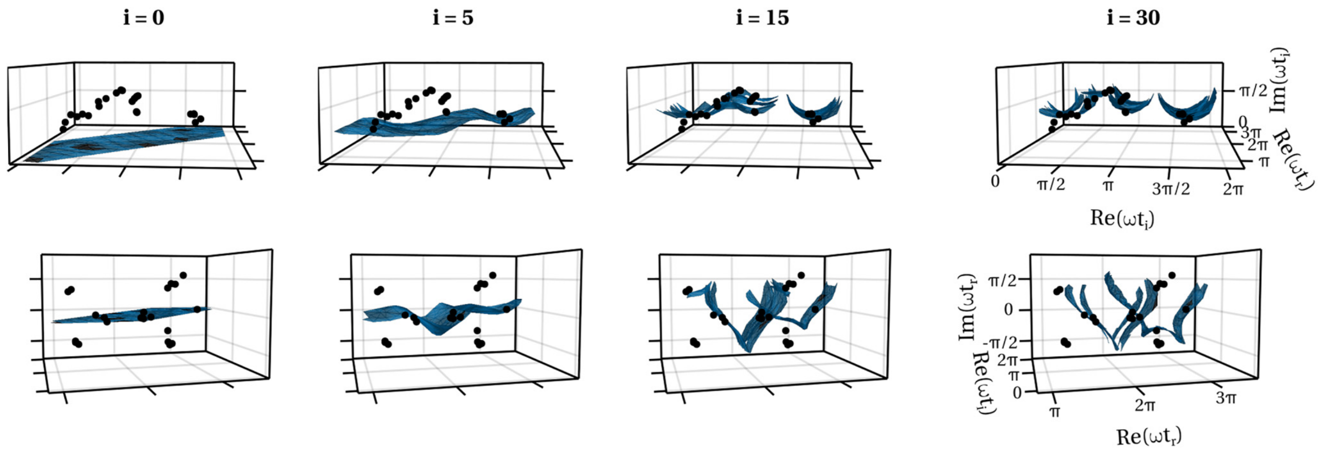

FIG. 11. Several steps of the deformation of the integration domain toward the Lefschetz thimble, shown in ionization-time projection (top row) and recombination-time projection (bottom row), for HHG driven by the two-color field shown in Fig. 1(b) and harmonic order $q = 25$.

3. *Comparison of the two methods: Harmonic spectra*

The resulting values of the integrals, in the form of spectral intensities (5) for a range of harmonic orders q, are shown in Fig. 12 for the monochromatic driving field (top panel) and the two-color field (bottom panel) as in Figs. 2(a) and 2(b), respectively. We show the Gaussian contribution from each saddle point in color (for relevant saddle points; light gray for noncontributing saddles). The coherent summation of relevant saddles' contribution is shown in black [saddle-point method, SPM, Eq. (9)], which is compared to the quadrature along the deformed integration contour [Picard–Lefschetz downward flow, PLDF, Eq. (29)] in blue. For the monochromatic driving field we recognize the familiar structure of a typical HHG spectrum exhibiting quantum-path interference. Throughout the spectrum there are two types of relevant contributions: from short and long trajectories (red and pink, respectively), of which the former become nonrelevant at the high-harmonic cutoff at $q_c = 42$. Note, small deviations between the two integration approaches only occur around this Stokes transition where the two saddle points are in close vicinity and their contribution should not be modeled as Gaussian, but rather as an Airy-type integral [54,56,57].

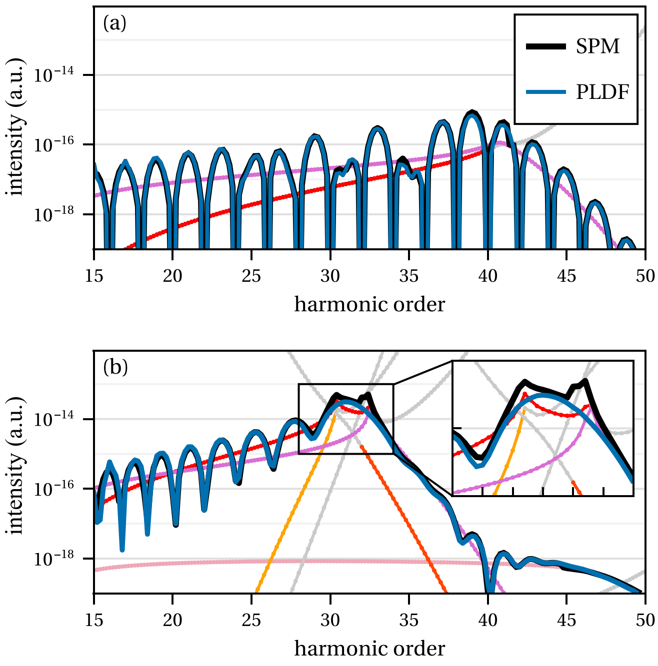

FIG. 12. HHG spectrum for the two fields shown in Fig. 1 [(a) for the monochromatic field in Fig. 1(a), (b) for the two-color field in Fig. 1(d)], calculated as a sum of Gaussian contributions from relevant saddle points (SPM, black line) as identified using the necklace algorithm, and as a quadrature of the deformed integration domain (PLDF, blue line). Individual saddle points' contributions are shown colored for relevant saddles, and gray for nonrelevant saddles. The bottom panel features an inset for the artificial discontinuity that arises for the SPM when saddle points are in close vicinity.

For the complicated two-color field [in Fig. 12(b)], the harmonic spectrum exhibits a more interesting structure, as we find more than only two types of trajectories. Throughout the first plateau (harmonic orders 15 to 32) we observe the expected interference structure from the two dominant trajectories marked in red and pink. However, we identify a more interesting feature of the spectrum that we can now attribute to individual trajectories, and which is shown enlarged in the inset. Around the first harmonic cutoff there are two other trajectories (yellow and orange) which contribute significantly to the integral and yield an overall spectral enhancement. This enhancement stems from the "cluster" of saddle points shown in Fig. 2(e) (panel D) and signifies the appearance of a caustic, which we address in more detail in the following section. In that region of the spectrum, the SPM exhibits both an artificial discontinuity and also the largest deviation from the PLDF-based signal. Again, this is expected, as for saddle points in close vicinity the integrand along the steepest-descent contour does not resemble a Gaussian. In these cases we can numerically integrate the individual saddles' steepest-descent thimbles, which provides an exact solution even in the case of fully coalescing saddle points at the caustic. A proper analytical treatment within saddle-point-based methods would require to develop a suitable uniform approximation to smoothen out the discontinuities. Within the PLDF method the integrand is directly evaluated along the thimble and agnostic of any saddle (or higher-order critical) points. That is, for example, in the event of a saddle-point coalescence, the respective thimbles will merge as well. As a result, the evaluated integral is naturally smooth throughout the spectrum and eliminates the need for a carefully constructed uniform approximation that connects different regimes of relevant saddle points. To this end, the PLDF provides a unique tool that captures the exact value of the integral while still allowing for a separation into distinct contributions from the disconnected components of the thimble, where each of them may be identified with a specific electron trajectory.

In the following section we demonstrate this key advantage of the integration along the thimbles by focusing on cases where saddle points lie in close vicinity, giving rise to caustics in the observables. In the subsequent section, we illustrate the capability of the necklace algorithm to identify relevant quantum orbits, on the example of the a parameter scan of amplitude ratios in two-color fields.

B. Spectral caustics

With the rigorous methods of Picard–Lefschetz theory, we can now study a phenomenon that has so far been inaccessible to semiclassical quantum-orbit analysis: caustics. Caustics are the bright features that appear whenever multiple classical solutions of a quantum-mechanical system coincide, as for example when multiple (classical) rays of sunlight are bent by the curved water surface onto the same position and cause a marbled pattern at the bottom of a swimming pool. In attosecond science, we find the same effect for specific shapes of the driving laser field's vector potential which causes the semiclassical electron trajectories to recombine at the same time and produce observable bright features in, for example, the HHG spectrum [12–17,107–109]. The most prominent example is the high-order harmonic cutoff, for which the saddle-point solutions for short and long trajectories are very close (or even coalesce) [57], and which was first observed as a divergence in the simpler, fully classical, "simple man's" model [18]. Mathematically, the appearance of caustics is linked to catastrophe theory (see Sec. III C) which relates the number of external parameters K to the number of coalescing saddle points $(K+1)$ and, hence, types of caustic structures and the degree of enhancement. In the context of HHG, the primary external parameters is the harmonic order q. Across a spectrum we can therefore observe features related to a fold catastrophe $(K=1)$ at which two saddle points coalesce [57].

As we increase the number of control parameters, e.g., by adding a second driving field, we can observe higher-order diffraction patterns (cf. [92], Sec. 36.3). Such bright features have been observed experimentally as intensity enhancements of specific harmonic orders in [12] and [14], where they have been attributed to a swallowtail catastrophe diffraction pattern and coinciding classical trajectories, respectively. Both experiments have slightly different parameters, but topologically they constitute the same situation: a HHG setup with a collinear two-color driver comprised of a fundamental field and a strong second-harmonic component. The caustics can then be found by scanning over phase delays between the two constituent fields and measuring the harmonic spectra. They are related to a swallowtail catastrophe point $(K=3)$, with the three external control parameters being harmonic order, phase delay, and relative intensity.

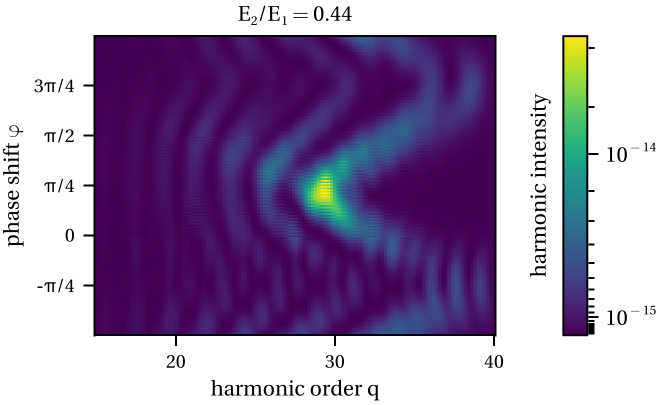

FIG. 13. Harmonic intensity (in a.u.) across a range of harmonic orders and phase shifts of the two-color field (30) with $E_2/E_1 = 0.44$, calculated using quadrature along the flowed integration domain (PLDF method), resembling a part of the canonical diffraction integral for a swallowtail catastrophe.

Here, we present the harmonic intensities for this setup across a scan over various phase delays φ between the two constituent fields, calculated using the PLDF method. That is, for every configuration of external parameters (φ, q) we deform the integration domain using the downward-flow algorithm to determine the Lefschetz thimbles and then evaluate the HHG dipole integral across the obtained thimble surface. In Fig. 13 we show this parameter scan for the electric field (30) with the fixed relative intensity $E_2/E_1 = 0.44$ that reveals a projection of the caustic pattern expected for a swallowtail catastrophe, and a significant enhancement around $q = 30$ and $\varphi = 0.59$.[14]

The Lefschetz thimbles for the parameters with highest intensity are shown in Fig. 14. While we cannot see striking differences in the ionization-time projection (top panel), we find a rather flat surface in the recombination-time projection (bottom panel). Comparing this to Fig. 11 where several saddle points' contributions yield "steep" and disconnected surfaces, this highlights the fact that around a swallowtail point multiple saddle points coalesce to one higher-order critical point for which the steepest-descent manifold covers a long range of recombination times.

Most importantly, this demonstrates our capability to evaluate the HHG dipole integral exactly, even around scenarios exhibiting caustic features. The specific setup showcased here is of particular interest as it reveals a significant enhancement of the harmonic response. However, for HHG driven by polychromatic fields it is not the only configuration where caustics appear, as, loosely speaking, each new frequency component of the driving field contributes new saddle-point solutions that may or may not coalesce (and hence produce caustics) in a specific parameter condition. One such caustic feature

---

[14] For comparison: in Fig. 2 in [12] the HHG yield was modeled as the respective canonical diffraction integral to demonstrate the expected pattern, and not actually calculated from the HHG integral.

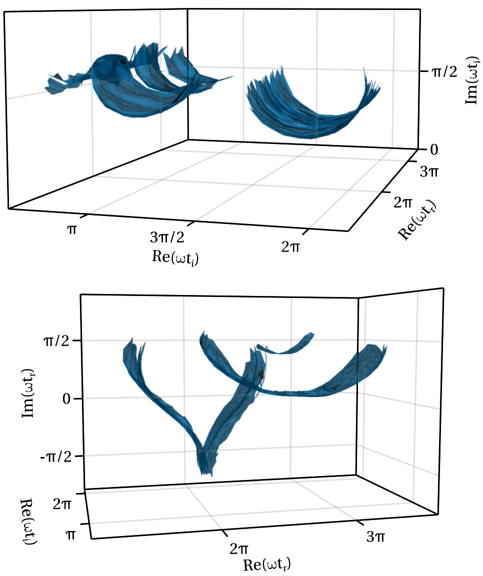

FIG. 14. Thimble for the HHG swallowtail configuration ($E_2/E_1 = 0.44$, $q = 30$, $\varphi = 0.59$), the most intense point of Fig. 13, in projections as in Fig. 11.

originating from the (near) coalescence of three saddle points to a cusp catastrophe point appears in the scenario presented in the following chapter, and is studied in more detail in the Appendix.

C. The color switchover

The necklace method introduced in Sec. III B 2 allows to determine relevant quantum orbits for any arbitrary driving field and independent of a classification of saddle-point solutions. This now enables us to answer the broader question of how quantum orbits develop throughout any (arbitrary!) smooth change of parameters. As an example, here we address the smooth change from a monochromatic driver, via a two-color field, to a monochromatic driver of second harmonic frequency—a technique we term color switchover (see evolution of field shapes in the left column of Fig. 15), and introduced in [42].

It provides a framework to study two-color driving fields with arbitrary intensity ratio (and phase shifts) that seamlessly connects perturbative setups (where the second color field intensity is in the order of a few percent) to fully bichromatic setups (with two constituent fields of equal intensity). This transition beyond the perturbative regime has proven to bear interesting dynamics in an ionization-only context already [42,110,111].

Here, we consider a color switchover with constant ponderomotive energy U_p,[15] i.e., constant total energy of the driving field. With that, the *classical* harmonic cutoff for a monochromatic driver, given by $q_\mathrm{class} \approx \mathcal{I}_\mathrm{p} + 3.17U_\mathrm{p}$, is the same for the beginning and end of the color switchover. We restrict our discussion to fields with zero phase delay ($\varphi = 0$) between the two components, such that the vector potential reads as

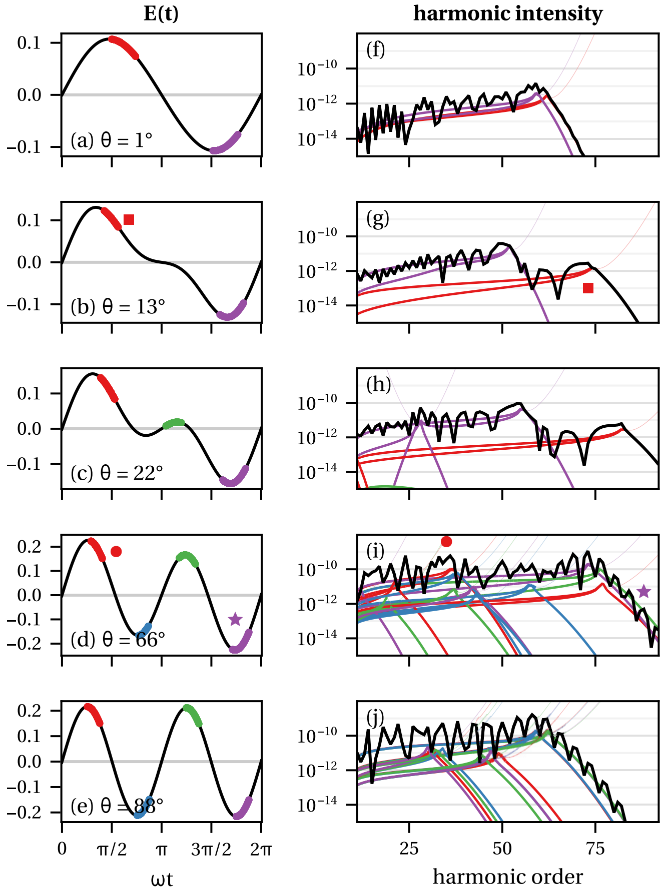

FIG. 15. The color switchover scheme: electric fields $E(t)$ (in a.u., left column) and respective HHG spectra $I(q\omega)$ (in a.u., right column) calculated as a sum of Gaussian contributions from relevant saddle points. Their individual contributions are color coded, based on their ionization times marked in the electric field. The markers in (g) and (i) indicate the specific contributions corresponding to the trajectories in Fig. 17.

$$A(t) = A_1\cos(\omega t) + A_2\cos(2\omega t),$$

$$\text{where}\quad A_1 = \cos(\theta)E_0/\omega \quad\text{and}\quad A_2 = \sin(\theta)E_0/(2\omega). \tag{35}$$

The electric field is hence given by

$$E(t) = E_1\sin(\omega t) + E_2\sin(2\omega t),$$

$$\text{where}\quad E_1 = E_0\cos(\theta) \quad\text{and}\quad E_2 = 2E_0\sin(\theta). \tag{36}$$

Here we have used the *mixing angle* θ as a parameter to tune the amplitude ratio of the two constituent fields as $E_2/E_1 = 2\tan\theta$. For $\theta = 0^\circ$ the field (36) corresponds to a monochromatic field with frequency ω, and for $\theta = 90^\circ$ to a monochromatic field with frequency 2ω. For all intermediate values of θ, Eq. (36) forms a two-color field with varying amplitude ratio.

On the left-hand column of Fig. 15. We show the total electric field $E(t)$ for the values $\theta = 1^\circ, 13^\circ, 22^\circ, 67^\circ$, and 88° in Figs. 15(a)–15(e), where we marked $\mathrm{Re}(t_{\mathrm{i},s})$ for

---

[15] The ponderomotive energy is the time-averaged quiver energy of the free electron over one cycle of the driving field, $U_\mathrm{p} = \langle E(t)\rangle_T = \frac{1}{4}({A_1}^2 + {A_2}^2)$.

contributing quantum orbits. This demonstrates the key intrigue of the scheme: At the initial stage of the switchover ($\theta = 1^\circ$) we have two (distinct and clearly separated) ionization bursts within one cycle of the fundamental T, just after the maxima of the field at $\omega t = \pi/2$ and $3\pi/2$ [Fig. 15(a)]. After the *continuous* transition to $\theta = 88^\circ$, however, we have four ionization bursts in that same time frame, around $\omega t = 0.6, 2.2, 3.8,$ and 5.3 [Fig. 15(e)]. Especially with the understanding that ionization events (and the associated recombination times, making them trajectories) correspond to saddle points, and saddle points are topologically stable features of analytic functions, this "jump" in number of ionization events raises a set of questions [42]: Where do the new ionization events come from? Which of the "old" trajectories correspond to the "new" ones? When do the new trajectories start to become relevant for the harmonic spectrum? Picard–Lefschetz theory allows us to answer these questions.

1. Saddle-point dynamics in complex time

Tracking how the saddle points move in the complex plane throughout the color switchover reveals rather complicated dynamics, which makes a consistent classification of trajectories tedious and nonunique, but still possible [76]. For example, in the beginning of the switchover the saddle points can be classified as "short" and "long" trajectories as shown in Figs. 2(b) and 2(c). Upon the color switchover the two "branches" may break up and reconnect with other, newly emerging, solutions, such that saddle points that would be classified as short trajectories for the monochromatic ω driving field transition smoothly (!) into being long trajectories.

The new saddle-point solutions mostly come in from high imaginary ionization times [note, e.g., the range of $\mathrm{Im}(t_{\mathrm{r},s})$ in Fig. 2(e) for ionization windows B and C] and move down toward the real axis until they are equally spread out. Focusing on the ionization times, we find that the typical structure around the first ionization burst around time $\omega t_{\mathrm{i}} = 1.9$ [as seen in Fig. 2(b)], "ripped apart" by the newly incoming saddle points, which subsequently push some solutions to earlier times and some solutions to later times. During this process, trajectories frequently undergo pairwise (avoided) crossings similar to the one observed and extensively described for the high-harmonic cutoff in Ref. [57]. As described therein, the full coalescence of two saddle points to a fold catastrophe point ($K = 1$) renders the classification ambiguous and introduces branch cuts into the unified Riemann surface that solves the saddle-point equations. For the performed color switchover considered here there are multiple instances of those full coalescences; we show one of them in Fig. 17(d) below.

2. Harmonic spectra throughout the switchover

Let us now highlight a few curious features that impact the observable harmonic spectrum. Therefore, in the right-hand side of Fig. 15 we present the harmonic spectra with their contributions from the individual saddle points for the respective stages of the color switchover. We colored the individual saddle points' contributions according to their ionization window indicated on the left-hand side, and we show the resulting total intensity [SPM, from Eq. (9)] in black. The contributions of nonrelevant saddle points are shown in faint lines.

For the initial stage of the color switchover, i.e., a purely monochromatic field with frequency ω, the HHG spectrum looks like the one shown in Fig. 12(a). The contributions from short and long trajectories from within in half-cycle interfere with each other and due to the dynamical symmetry of the driving field result in the cancellation of the odd-order total intensities. A slight perturbation to the driving field breaks this behavior. In Figs. 15(a) and 15(f) we show the field and the resulting spectrum shortly after the initial stage of the color switchover ($\theta = 1^\circ$), i.e., a two-color driving field with a weak 2ω component. We see that the comblike structure of Fig. 12(a) is broken. Moreover, the contributions of short-long pairs from within each half-cycle start to separate, visible at the harmonic cutoff (here around order 60).

When increasing the strength of the second-color field [Figs. 15(g)–15(j)], this spreading becomes more pronounced. The newly incoming saddle-point solutions ultimately cause the harmonic cutoff in the spectrum to break up into two visible cutoffs [around $q = 50$ and 75 in Fig. 15(g)]. For the later stage of the color switchover the newly emergent trajectories produce multiple cutoffs, in Fig. 15(j) at $q \approx 32$, 47, and 60. The former, however, do not impact the total shape of the harmonic spectrum as they stem from higher-order return pairs of saddle points, i.e., trajectories with longer travel times and hence weaker contribution [97].

Upon the full completion of the color switchover we also restore the expected suppression of odd harmonic orders (of the 2ω driver) due to the symmetry of the driving field.

3. Spectral enhancements at the cusp catastrophe

The quantum-orbit-based consideration of the color switchover allows us to study the intriguing interplay of more than two trajectories. For example, the color switchover presented here entails an avoided crossing of three trajectories. Even if the chosen parameter scan does not include an exact coalesce,[16] it nevertheless results in an enhanced signal for specific harmonic orders, depending on the mixing angle. This can be seen in Fig. 15(h) around $q = 28$, where we find three contributing saddle-point contributions in close vicinity (see the three purple lines) resulting in a noticeable increase of the total spectral intensity around this harmonic order. A more detailed analysis of this cusp catastrophe point is shown in Appendix.

In Fig. 16 we show the corresponding semiclassical electron trajectories for the respective three saddle points for this situation, as well as for a subsequent field configuration in the switchover, at $\theta = 45^\circ$, for comparison. The trajectories are described by the displacement from the origin (the nucleus)

$$\mathbf{x}(t) = \int_{t_{\mathrm{i},s}}^{t_{\mathrm{r},s}} [\mathbf{p}_s + \mathbf{A}(t)]\,\mathrm{d}t, \tag{37}$$

---

[16] In fact, the exact coalescence of multiple saddle points requires complex-valued external parameters, as is explained in full detail for the case of the coalescence of two saddle points at the high-harmonic cutoff in [57].

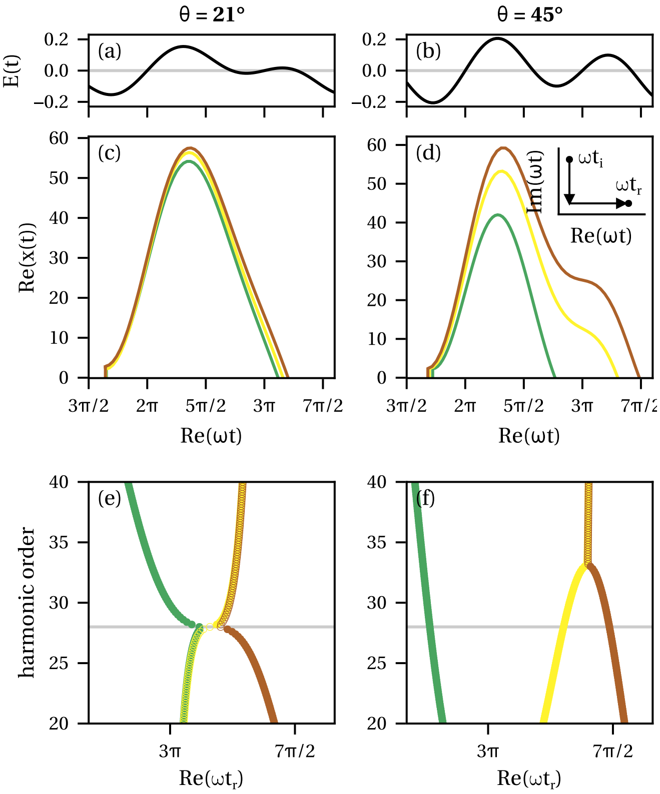

FIG. 16. Electric fields [(a) and (b)] and three according semiclassical electron trajectories [(c) and (d)] for three saddle points contributing to harmonic order $q = 28$. The respective energy-time relations are shown in (e) and (f), where filled (empty) markers are (non-)relevant saddle points. The three assimilating trajectories for $\theta = 21^\circ$ ($E_2/E_1 = 0.78$) on the left-hand side cause the enhancement seen in the respective spectrum, Fig. 15(h). The temporal contour along which the integral (37) is evaluated is shown in the inset of (d).

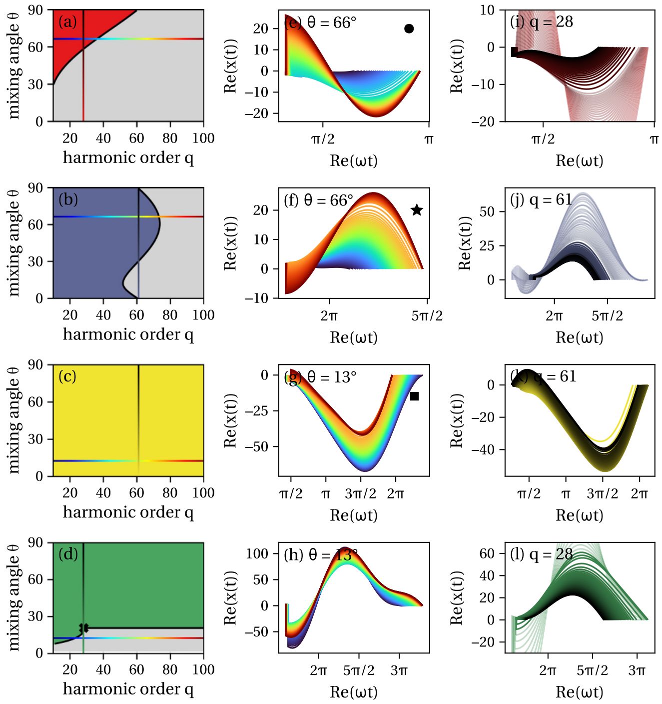

FIG. 17. Tracking four different saddle points (rows) throughout the color switchover and harmonic orders. Left column: showing whether the saddle point is relevant (colored) or not (gray). Center column: trajectories according to Eq. (37) for the indicated θ value (horizontal line in the left panel), for all harmonic orders (lines colored, respectively). Right column: trajectories for the indicated harmonic order (vertical line in the left panel), throughout the color switchover (i.e., all values of θ, color shaded, respectively). Markers in (e), (f), and (g) attribute contributions to the spectra in Figs. 15(j) and 15(g).

where the temporal integration starts from $t_{\mathrm{i},s} \in \mathbb{C}$ and goes down to $\mathrm{Re}(t_{\mathrm{i},s})$, then all the way to $\mathrm{Re}(t_{\mathrm{r},s})$ where it terminates at $t_{\mathrm{r},s} \in \mathbb{C}$, shown as an inset in Fig. 16. The first leg of this contour can be interpreted as the trajectory inside the tunneling barrier and it will give an imaginary-valued displacement $\mathbf{x}(t)$. The second part of the time contour then describes the classical path of the electron under the influence of the driving laser field [49,101]. In Fig. 16(c) the trajectories for the cusp situation are nearly merging, whereas for a subsequent field configuration [Fig. 16(d)] the trajectories are noticeably different.

Phenomenologically, this is the same situation as in the swallowtail caustic described above. For most scenarios all the various electron trajectories interfere destructively and their contributions "counteract" each other. In situations like Fig. 16(b), the depicted electron pathways lie so close together—while still being individually relevant contributions—that they interfere constructively as they all contribute with the same phase towards the total HHG dipole. This results in a significant enhancement compared to other configurations. Technically, this is exactly the phenomenon that can be used to optimize the spectral yield of a desired harmonic order [14].

4. Individual quantum orbits throughout the switchover

Apart from looking at the shape of the total harmonic response and how the several ionization windows interfere, the necklace algorithm gives us the unique capability to follow individual quantum orbits throughout the color switchover. This has been inaccessible within the existing understanding of saddle-point methods or their extension to uniform approximations. In particular, tracking saddle points allows to examine how the respective electron trajectories and their relevance to the spectrum changes. In Fig. 17 we showcase four (types of) saddle points in detail, as representative examples of common behaviors. In the left column we show whether the respective saddle point is relevant (colored) or not (gray), as it is tracked for the range of harmonic orders and throughout the color switchover. Hence, the boundary of the colored region of contributions are the Stokes lines in parameter space, drawn as a black line. In the second column we show the specific semiclassical electron trajectories, for a fixed mixing angle (indicated with the rainbow-colored horizontal line in the left panel) and a range of harmonic orders denoted with the respective color. Similarly, the third column shows the trajectories for a fixed harmonic order (indicated by the vertical bar in the left panel) and across the color switchover denoted with the color gradient. For nonrelevant trajectories the lines are drawn faint where it does not lead to confusion.

The first row in Fig. 17 shows what is eventually the most dominant short trajectory for the first ionization window of the 2ω field. That is, from Fig. 17(a) we find that for $\theta = 90^\circ$ this saddle point is relevant up to harmonic order $q \approx 60$, which constitutes the cutoff of Fig. 15(j). Prior to that (for $\theta < 90^\circ$), this saddle point only contributes for lower harmonic orders, or not at all. We find this behavior particularly interesting, as this saddle point only starts contributing quite late in the color switchover, but then in fact plays a prominent role for the spectrum of the fully 2ω driving field. The trajectories shown in the center panel (for all harmonic orders) correspond to the contribution marked with a circle in the harmonic spectrum in Fig. 15(i).

In contrast to that, the trajectory showcased in the second row contributes to (at least) the early plateau throughout the full color switchover. It is the first, and hence most dominant, short trajectory starting from ionization burst four, marked in Fig. 15(i) with a star. This trajectory remains one of the most dominant contributors to the spectrum throughout the color switchover, so that its Stokes line marks a noticeable cutoff in the spectrum. The Stokes line in the left panel explains the shift in the high-order harmonic cutoff observed from orders $q = 60$ for $\theta = 0$ to 75, 82, 78, and 60 for 13°, 22°, 67°, and 88° as seen in Figs. 15(f)–15(j), respectively.

In the third row we show the first long trajectory of the second ionization burst of the 2ω driver around $\omega t_\mathrm{i} = 2.22$, marked in Figs. 15(b) and 15(g) with a square. As a long trajectory it is relevant for all harmonic orders and remains so throughout the whole color switchover.

The trajectory shown in the last row is involved in the caustic mentioned to explain the enhancement around $q = 28$ in Fig. 15(h). Around the caustic there is a saddle-point coalescence that introduces ambiguity in the classification and shows up as a clear discontinuity in Fig. 17(d). For the beginning of the color switchover this saddle point was a higher-order return trajectory. After this branch cut, however, this trajectory eventually becomes the long trajectory of the fourth ionization burst of the 2ω field.

To conclude, Fig. 17 demonstrates how the electron trajectories change smoothly upon parameter scans, but their relevance to the total spectrum may change abruptly. In turn, tracking contributions from distinct quantum orbits throughout a parameter scan allows us to attribute the observable features of the harmonic spectra to these specific saddle-point dynamics.

V. OUTLOOK

This paper introduces the ideas of Picard–Lefschetz theory to attosecond science and strong-field physics. We presented two computational methods that utilize these concepts: the continuous downward flow of the integration domain, and the necklace algorithm to determine the relevance of given saddle points. Both of those methods have the flow of the discretized integration domain [Eqs. (12) and (22), or (32) and (34) in the context of HHG] as a central algorithmic element. While these flows theoretically preserve $\mathrm{Im}[\phi(x)]$, their discretized numerical implementation as a first-order Euler scheme can lead to numerical instabilities and, hence, limitations in the usage of the methods. This issue becomes particularly important near Stokes transitions, where a precise treatment of $\mathrm{Im}[\phi(x)]$ is essential by definition. Looking forward, a more rigorous way to identify and incorporate Stokes transitions can be developed.

We have applied our methods to calculate the HHG response across ranges of external parameters that contain Stokes transitions and hence show caustics. Generally, the study of caustics is inherently linked to the framework of catastrophe theory. By identifying parameters that cause the coalescence of saddle points one can hence classify the respective catastrophe. This allows us to compute the expected enhancement of the signal at the catastrophe point compared to the signal in its vicinity. The so-called "twinkling exponents" [112] have been used to motivate the enhancements within a harmonic spectrum [12,14], but the rigorous derivation for arbitrary parameter scans is still missing in the context of attosecond experiments.

Furthermore, the identification of catastrophe points allows to develop uniform approximations that smoothen the integral contribution of several saddle points in its parameter vicinity. Realizing these for specific parameter scans would allow a fully saddle-point-based analytical approach without artificial discontinuities even in the case of coalescences of three or more saddle points.

Alternatively, however, the separate thimbles can be evaluated individually using a standard quadrature of the surface elements. As shown by Eq. (29) this yields the exact integral for the HHG dipole in terms of distinct contributions, irrespective of the saddle points (and their vicinity).

VI. CONCLUSION

The description of strong-field-induced processes like tunnel ionization and the generation of high-order harmonics is often linked to the intuitive picture of interfering semiclassical electron trajectories. Mathematically, this corresponds to making the saddle-point approximation to the integrals that describe the atomic response in the SFA formulation, such as the harmonic radiation dipole (6). The spectral intensity of a given harmonic order is expressed as a sum over contributions from discrete quantum orbits, i.e., a sum of Gaussians centered around saddle points. For a given laser field, however, there are far more solutions to the saddle-point equations (10) than quantum orbits that contribute to the dynamics. Their selection has so far been based on heuristics and empirical rules, which fail for generic state-of-the-art lasers to drive the process.

In this paper, we presented Picard–Lefschetz theory as a tool to rigorously and unambiguously evaluate the dipole response in a quantum-orbit-based fashion for any arbitrary driving laser waveforms. For that, we understand the dipole response as a two-dimensional path integral over ionization and recombination times. Continuously deforming the two-dimensional integration contour into the complex plane allows to rewrite the integral as a sum of contributions along so-called Lefschetz thimbles. These are steepest-descent contours (surfaces) attached to the saddle points. The continuous deformation of the contour towards the thimble is dictated by the “downward flow” and preserves the value of the integral, such that any intermediate flow step is an equal, and hence exact, representation of the integral. Conversely, as an alternative approach, we can identify contributing saddle points by checking whether there is an “upward flow” (a steepest-ascent contour, the dual thimble) that connects them back to the original integration domain, the plane of real ionization and recombination times. For the case of a one-dimensional integral the steepest-ascent contours are lines that connect back to the real axes for relevant saddle points—a property that is computationally straightforward to inspect. For the case of a two-dimensional integral the steepest-ascent contours are surfaces (embedded in 4D real space) which cannot be readily determined. We therefore introduced a procedure that we call the necklace algorithm, in which we only flow the brim of the dual thimble and indubitably identify all possible intersections with the real plane. This allows us to systematically determine relevant saddle points to a two-dimensional integral.

We apply these methods to strong-field phenomena that have so far been inaccessible to semiclassical analysis. One of them is the appearance of spectral caustics, where the close proximity (or even the full coalescence) of multiple saddle-point solutions (read trajectories) causes a significant enhancement in the observed signal. In these scenarios, the correct analytical representation of the integral requires uniform approximations that account for the non-Gaussian shape around the saddle points. Evaluating the integrand along the deformed contour, however, is independent of the nature of the critical points, and hence allows us to evaluate the SFA integral exactly even in the vicinity of saddle-point coalescences.

The versatility of the introduced Picard–Lefschetz methods allows us furthermore to address questions of a new class of parameter scans: the color switchover [42]. The gradual replacement of a monochromatic driving field with its second harmonic, via two-color configurations of increasing amplitude ratio, connects the perturbative second-color regime to fully bichromatic driving fields. Using the necklace algorithm, we are able to identify the relevant quantum orbits throughout the full range of different driving-field configurations. For the perturbative case, we can attribute the unfolding of the high-harmonic cutoff to the dominant pairs of trajectories from the respective half-cycles. Increasing the relative strength of the second harmonic eventually leads to newly emerging ionization bursts that produce topologically stable enhancements in the spectrum. These arise due to the unavoidable proximity to a threefold saddle-point coalescence (a cusp catastrophe), which is here demonstrated in the context of attosecond science. Moreover, tracking individual saddle-point solutions throughout the color switchover allows to show how the electron trajectories react to the change of driving field.

Ultimately, we have shown the rigorous link between the SFA integrals for both the ionization amplitude (one-dimensional time integral) and the HHG response (two-dimensional), and its interpretation in terms of quantum orbits, for arbitrary driving fields. This opens up the possibility to analyze semiclassical trajectories for generic parameter scans and more complex wave forms, e.g., three-dimensionally structured light fields. Depending on the specific configuration, there might be other methods derived from Picard–Lefschetz theory that simplify the identification of relevant quantum orbits or, more generally, the evaluation of the integral. More specifically, the relevance of quantum orbits and the occurrence of Stokes phenomena may be further illuminated by including higher-order corrections in the saddle-point approximation using the mathematical theory of resurgence [113,114]. Furthermore, we look forward to seeing Picard–Lefschetz methods applied to other highly oscillatory integrals within attosecond science as well, including high-order ATI, with its description of rescattered electrons [53,65,66], dynamic interference in ionization stabilization [115,116], or attosecond streaking [117]. As the theoretical framework is independent of the dimensionality of the integral, it could be used to simplify the five-dimensional integrals arising in calculating the response of solid targets to strong laser-field radiation [118].

ACKNOWLEDGMENTS

We wish to acknowledge Iain Murray for encouraging this interdisciplinary collaboration between A.W. and J.F. A.W. and E.P. acknowledge Royal Society funding under Grants No. URF\R1\211390 and No. RF\ERE\210255. The work of J.F. is supported by the STFC Consolidated Grant Particle Physics at the Higgs Centre, and, respectively, by a Higgs Fellowship at the University of Edinburgh.

DATA AVAILABILITY

The data that support the findings of this article are openly available in Ref. [46].

APPENDIX: THE CUSP CATASTROPHE POINT

As a topological feature of the color switchover we identify a cusp catastrophe point causing observable enhancements in the spectrum. For the exact coalescence of three saddle points, however, we require external parameters to assume complex values. The smaller those imaginary parts are, the larger is the effect of the catastrophe point on the observed quantity. For

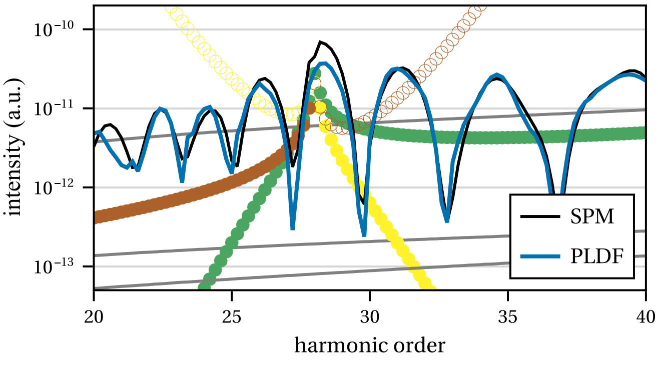

FIG. 18. Zoom-in on the spectrum of Fig. 15(h), highlighting the three different contributions that cause the enhancement of harmonic order 28 due to the nearby cusp catastrophe point. The saddle-point method (black, SPM) shows a discontinuity at this enhancement, whereas the Picard–Lefschetz downward flow (blue, PLDF) remains smooth across the caustic. Individual saddle points’ contributions are shown as (empty) filled markers for the (non-)relevant saddle points that are involved in the caustic.

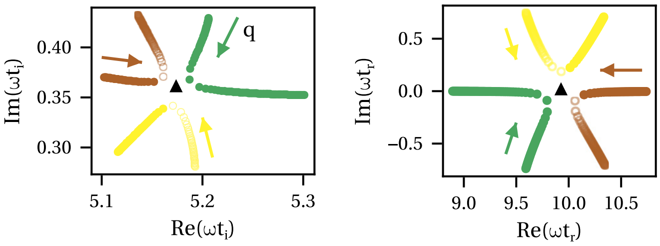

FIG. 19. Saddle points in the complex plane for the spectrum shown in Fig. 15(h), indicating a cusp catastrophe.

the given phase shift $\varphi = 0$ presented in the main text of this paper we find the largest relative enhancement of this cusp point when $\theta = 21^\circ$ (see Fig. 18). At the enhancement around harmonic order $q \approx 28$, we find a slight discontinuity in the harmonic intensity as calculated from the sum over relevant saddle points (black, SPM). In contrast, the total intensity calculated using the downward flow (blue, PLDF) remains smooth across this caustic.

The saddle points for $\theta = 21^\circ$ ($E_2/E_1 = 0.78$), $\varphi = 0$, and for a range of $q = 20$ to 40 are shown in Fig. 19, indicating three branches of solutions in close proximity. The exact coalescence for three solutions only happens in complex parameter space, at $\theta = (21.28 + 0.03i)^\circ$, $\varphi = 0$, and $q = 27.95–0.1i$. This cusp point is marked as a triangle in Fig. 19, sitting in the center of the three real-parameter saddle points.

In Fig. 20 we show how the exact location of this cusp point changes depending on the external parameters. The [Re(q), Re(θ)] projection in Fig. 20(b) indicates how the specific harmonic order which is enhanced by the coalescence changes as we perform the color switchover. Figure 20(c) confirms that for color switchovers with a different two-color phase delay φ there is still a cusp catastrophe point [76]. However, the increased imaginary parts of the external parameters (indicated by the marker size) suggest that it plays a subdominant role for the total spectrum.

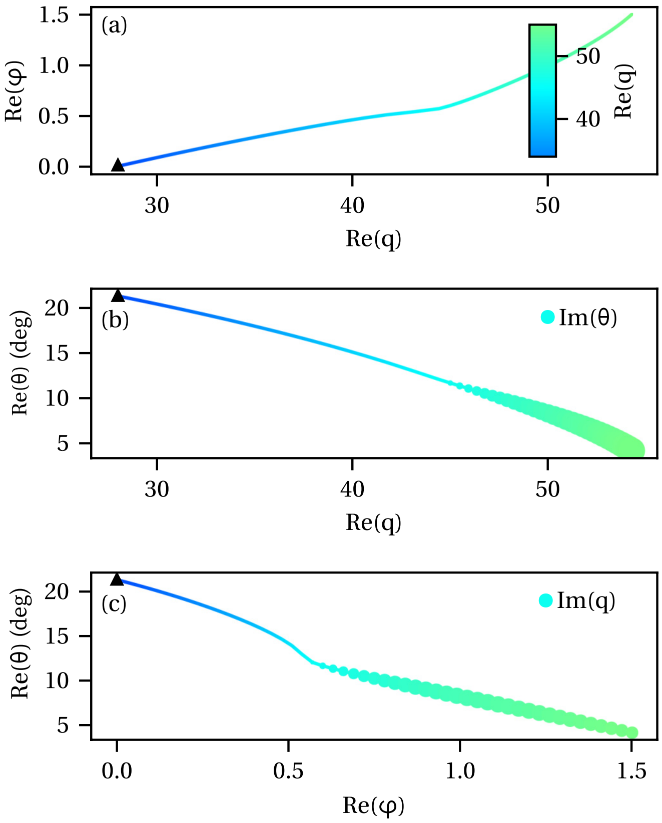

FIG. 20. Projections of parameter combinations (θ, φ, q) for a cusp catastrophe point at which three saddle points coalesce. For the exact coalescence we assume $\theta \in \mathbb{C}$ and $q \in \mathbb{C}$ and denote the respective imaginary parts as marker size in (b) and (c). In all three panels the color indicates the real part of the harmonic order q. The cusp point reported in the main text and above is drawn as a triangle.

---

[1] M. Lewenstein, Theory of high-harmonic generation by low-frequency laser fields, Phys. Rev. A **49**, 2117 (1994).

[2] L. Keldysh, Ionization in the field of a strong electromagnetic wave, Zh. Eksp. Teor. Fiz. **47**, 1945 (1965) [Sov. Phys.–JETP **20**, 1307 (1965)].

[3] A. Perelomov, V. Popov, and M. Terent'ev, Ionization of atoms in an alternating electric field: II, Zh. Eksp. Teor. Fiz. **51**, 309 (1967) [Sov. Phys.–JETP **24**, 207 (1967)].

[4] W. Becker, F. Grasbon, R. Kopold, *et al.*, Above-threshold ionization: From classical features to quantum effects, in *Advances In Atomic, Molecular, and Optical Physics*, edited by B. Bederson and H. Walther (Academic, New York, 2002), Vol. 48, pp. 35–98.

[5] R. Kopold, W. Becker, and M. Kleber, Quantum path analysis of high-order above-threshold ionization, dedicated to Marlan O. Scully on the occasion of his 60th birthday, Opt. Commun. **179**, 39 (2000).

[6] P. Salières, B. Carré, L. Le Déroff, *et al.*, Feynman's path-integral approach for intense-laser-atom interactions, Science **292**, 902 (2001).

[7] S. Lefschetz, *L'Analysis Situs et la Géométrie Algébrique* (Gauthier-Villars, Paris, 1924).

[8] E. Picard and G. Simart, *Théorie des Fonctions Algébriques de Deux Variables Indépendantes* (Gauthier-Villars, Paris, 1897).

[9] F. Pham, Vanishing homologies and the n variables saddle-point method, in *Singularities, Part 2* (American Mathematical Society, Providence, RI, 1983), pp. 310–333.

[10] E. Witten, Analytic continuation of Chern-Simons theory, AMS/IP Stud. Adv. Math. **50**, 347 (2011).

[11] J. Feldbrugge and N. Turok, Existence of real time quantum path integrals, Ann. Phys. **454**, 169315 (2023).

[12] O. Raz, O. Pedatzur, B. D. Bruner, and N. Dudovich, Spectral caustics in attosecond science, Nat. Photon. **6**, 170 (2012).

[13] V. A. Birulia and V. V. Strelkov, Spectral caustic in two-color high-order harmonic generation: Role of Coulomb effects, Phys. Rev. A **99**, 043413 (2019).

[14] A.-K. Raab, M. Redon, S. R. Abbing, *et al.*, XUV yield optimization of two-color high-order harmonic generation in gases, Nanophotonics **14**, 3947 (2025).

[15] F. Dong, Q. Xia, and J. Liu, Caustic effects on high-order harmonic generation in graphene, Phys. Rev. A **109**, L041102 (2024).

[16] D. Faccialà, S. Pabst, B. D. Bruner, *et al.*, High-order harmonic generation spectroscopy by recolliding electron caustics, J. Phys. B: At. Mol. Opt. Phys. **51**, 134002 (2018).

[17] D. Faccialà, S. Pabst, B. D. Bruner, *et al.*, Probe of multielectron dynamics in xenon by caustics in high-order harmonic generation, Phys. Rev. Lett. **117**, 093902 (2016).

[18] P. B. Corkum, Plasma perspective on strong field multiphoton ionization, Phys. Rev. Lett. **71**, 1994 (1993).

[19] K. C. Kulander, K. J. Schafer, and J. L. Krause, Dynamics of short-pulse excitation, ionization and harmonic conversion, in *Super-Intense Laser–Atom Physics*, NATO ASI Series (Springer, New York, NY, 1993), pp. 95–110.

[20] C. Jin, G. Wang, H. Wei, *et al.*, Waveforms for optimal sub-keV high-order harmonics with synthesized two- or three-color laser fields, Nat. Commun. **5**, 4003 (2014).

[21] G. Cirmi, R. E. Mainz, M. A. Silva-Toledo, *et al.*, Optical waveform synthesis and its applications, Laser Photon. Rev. **17**, 2200588 (2023).

[22] S. Mitra, S. Biswas, J. Schötz, *et al.*, Suppression of individual peaks in two-color high harmonic generation, J. Phys. B: At. Mol. Opt. Phys. **53**, 134004 (2020).

[23] E. Mansten, J. M. Dahlström, P. Johnsson, *et al.*, Spectral shaping of attosecond pulses using two-color laser fields, New J. Phys. **10**, 083041 (2008).

[24] L. E. Chipperfield, J. S. Robinson, J. W. G. Tisch, and J. P. Marangos, Ideal waveform to generate the maximum possible electron recollision energy for any given oscillation period, Phys. Rev. Lett. **102**, 063003 (2009).

[25] O. Kneller, D. Azoury, Y. Federman, *et al.*, A look under the tunnelling barrier via attosecond-gated interferometry, Nat. Photonics **16**, 304 (2022).

[26] X. He, J. M. Dahlström, R. Rakowski, *et al.*, Interference effects in two-color high-order harmonic generation, Phys. Rev. A **82**, 033410 (2010).

[27] D. Shafir, H. Soifer, B. D. Bruner, *et al.*, Resolving the time when an electron exits a tunnelling barrier, Nature (London) **485**, 343 (2012).

[28] N. Dudovich, O. Smirnova, J. Levesque, *et al.*, Measuring and controlling the birth of attosecond XUV pulses, Nat. Phys. **2**, 781 (2006).

[29] J. Zhao and M. Lein, Determination of ionization and tunneling times in high-order harmonic generation, Phys. Rev. Lett. **111**, 043901 (2013).

[30] N. Eicke and M. Lein, Attoclock with counter-rotating bicircular laser fields, Phys. Rev. A **99**, 031402 (2019).

[31] J. Mauritsson, J. M. Dahlström, E. Mansten, and T. Fordell, Sub-cycle control of attosecond pulse generation using two-colour laser fields, J. Phys. B: At. Mol. Opt. Phys. **42**, 134003 (2009).

[32] C. Ruiz, D. J. Hoffmann, R. Torres, *et al.*, Control of the polarization of attosecond pulses using a two-color field, New J. Phys. **11**, 113045 (2009).

[33] S. Roscam Abbing, F. Campi, F. S. Sajjadian, *et al.*, Divergence control of high-harmonic generation, Phys. Rev. Appl. **13**, 054029 (2020).

[34] S. Haessler, T. Balčiunas, G. Fan, *et al.*, Optimization of quantum trajectories driven by strong-field waveforms, Phys. Rev. X **4**, 021028 (2014).

[35] D. Baykusheva and H. J. Wörner, Chiral discrimination through bielliptical high-harmonic spectroscopy, Phys. Rev. X **8**, 031060 (2018).

[36] D. Ayuso, O. Neufeld, A. F. Ordonez, *et al.*, Synthetic chiral light for efficient control of chiral light–matter interaction, Nat. Photon. **13**, 866 (2019).

[37] J. Feldbrugge, J.-L. Lehners, and N. Turok, Lorentzian quantum cosmology, Phys. Rev. D **95**, 103508 (2017).

[38] Y. Tanizaki and T. Koike, Real-time Feynman path integral with Picard–Lefschetz theory and its applications to quantum tunneling, Ann. Phys. **351**, 250 (2014).

[39] R. Bharathkumar and A. Joseph, Lefschetz thimbles and quantum phases in zero-dimensional bosonic models, Eur. Phys. J. C **80**, 923 (2020).

[40] J. Feldbrugge, U.-L. Pen, and N. Turok, Oscillatory path integrals for radio astronomy, Ann. Phys. **451**, 169255 (2023).

[41] J. Feldbrugge and J. Y. L. Jones, Efficient evaluation of real-time path integrals, Phys. Rev. D **111**, 083524 (2025).

[42] A. Weber, M. Khokhlova, and E. Pisanty, Quantum tunneling without a barrier, Phys. Rev. A **111**, 043103 (2025).

[43] A. Weber, PicardLefschetz.jl, https://github.com/anneaux/PicardLefschetz.jl, Zenodo, 2026, doi:10.5281/zenodo.18504409.

[44] A. Weber, ATIsimPL, https://github.com/anneaux/ATIsimPL, Zenodo, 2026, doi:10.5281/zenodo.18504217.

[45] A. Weber, HHGsimPL, https://github.com/anneaux/HHGsimPL, Zenodo, 2026, doi:10.5281/zenodo.18504394.

[46] A. Weber, Figure-maker notebooks and code for Picard–Lefschetz methods for ATI and HHG integrals, Zenodo, 2026, doi:10.5281/zenodo.17298777.

[47] A.-T. Le, H. Wei, C. Jin, and C. D. Lin, Strong-field approximation and its extension for high-order harmonic generation with mid-infrared lasers, J. Phys. B: At. Mol. Opt. Phys. **49**, 053001 (2016).

[48] S. V. Popruzhenko, Keldysh theory of strong field ionization: History, applications, difficulties and perspectives, J. Phys. B: At. Mol. Opt. Phys. **47**, 204001 (2014).

[49] O. Smirnova and M. Ivanov, Multielectron high harmonic generation: Simple man on a complex plane, in *Attosecond and XUV Physics: Ultrafast Dynamics and Spectroscopy*, edited by T. Schultz and M. Vrakking (Wiley, Weinheim, 2014), pp. 201–256.

[50] K. Amini, J. Biegert, F. Calegari, *et al.*, Symphony on strong field approximation, Rep. Prog. Phys. **82**, 116001 (2019).

[51] N. Bleistein and R. A. Handelsman, *Asymptotic Expansions of Integrals* (Ardent Media, Ottawa, 1975).

[52] R. Wong, *Asymptotic and Computational Analysis: Conference in Honor of Frank W.J. Olver's 65th Birthday* (CRC Press, Boca Raton, FL, 2020).

[53] A. Jašarević, E. Hasović, R. Kopold, *et al.*, Application of the saddle-point method to strong-laser-field ionization, J. Phys. A: Math. Theor. **53**, 125201 (2020).

[54] D. B. Milošević and W. Becker, Role of long quantum orbits in high-order harmonic generation, Phys. Rev. A **66**, 063417 (2002).

[55] C. Figueira de Morisson Faria, D. B. Milošević, and G. G. Paulus, Phase-dependent effects in bichromatic high-order harmonic generation, Phys. Rev. A **61**, 063415 (2000).

[56] C. Figueira de Morisson Faria, H. Schomerus, and W. Becker, High-order above-threshold ionization: The uniform approximation and the effect of the binding potential, Phys. Rev. A **66**, 043413 (2002).

[57] E. Pisanty, M. F. Ciappina, and M. Lewenstein, The imaginary part of the high-harmonic cutoff, J. Phys.: Photonics **2**, 034013 (2020).

[58] D. B. Milošević, Application of the uniform approximation to integrals occurring in ionization by a strong elliptically polarized laser field, Phys. Rev. A **111**, 053105 (2025).

[59] D. Habibović and D. B. Milošević, Complete classification and additional saddle-point solutions for high-order above-threshold ionization induced by a strong laser field, Phys. Rev. A **111**, 023103 (2025).

[60] A. Gibbs, D. P. Hewett, and D. Huybrechs, Numerical evaluation of oscillatory integrals via automated steepest descent contour deformation, J. Comput. Phys. **501**, 112787 (2024).

[61] A. V. Shanin, A. I. Korolkov, and K. S. Kniazeva, Saddle point method for transient processes in waveguides, J. Theor. Comp. Acout. **30**, 2150018 (2022).

[62] F. H. M. Faisal, Multiple absorption of laser photons by atoms, J. Phys. B: At. Mol. Phys. **6**, L89 (1973).

[63] H. R. Reiss, Effect of an intense electromagnetic field on a weakly bound system, Phys. Rev. A **22**, 1786 (1980).

[64] A. Nayak, M. Dumergue, S. Kühn, *et al.*, Saddle point approaches in strong field physics and generation of attosecond pulses, Phys. Rep. **833**, 1 (2019).

[65] D. B. Milošević, D. Bauer, and W. Becker, Quantum-orbit theory of high-order atomic processes in intense laser fields, J. Mod. Opt. **53**, 125 (2006).

[66] D. B. Milošević and W. Becker, X-ray harmonic generation by orthogonally polarized two-color fields: Spectral shape and polarization, Phys. Rev. A **100**, 031401 (2019).

[67] V. I. Arnold, A. N. Varchenko, and S. M. Gusein-Zade, *Singularities of Differentiable Maps: Volume II Monodromy and Asymptotic Integrals* (Birkhäuser, Basel, 2012).

[68] J. Feldbrugge, J.-L. Lehners, and N. Turok, No smooth beginning for spacetime, Phys. Rev. Lett. **119**, 171301 (2017).

[69] J. Feldbrugge, Multiplane lensing in wave optics, Mon. Not. R. Astron. Soc. **520**, 2995 (2023).

[70] B. Bonga, J. Feldbrugge, and A. R. Metidieri, Wave optics for rotating stars, Phys. Rev. D **111**, 063061 (2025).

[71] H. Fujii, D. Honda, M. Kato, *et al.*, Hybrid Monte Carlo on Lefschetz thimbles – A study of the residual sign problem, J. High Energy Phys. 10 (2013) 147.

[72] M. Cristoforetti, F. D. Renzo, and L. Scorzato (Collaboration, AuroraScience), High density QCD on a Lefschetz thimble? Phys. Rev. D **86**, 074506 (2012).

[73] M. Cristoforetti, F. D. Renzo, A. Mukherjee, and L. Scorzato, Monte Carlo simulations on the Lefschetz thimble: Taming the sign problem, Phys. Rev. D **88**, 051501 (2013).

[74] J. Feldbrugge and U.-L. Pen, The real-time Feynman path integral for step potentials, Ann. Phys. **490**, 170490 (2026).

[75] J. Feldbrugge, D. L. Jow, and U.-L. Pen, Complex classical paths in quantum reflections and tunneling, Phys. Rev. D **111**, 085027 (2025).

[76] A. Weber, Caustics and catastrophes in strong-field physics. Picard–Lefschetz theory as a universal approach to saddle-point methods in attosecond science, Ph.D. thesis, King's College London, 2026, arXiv:2605.03794, https://kclpure.kcl.ac.uk/portal/en/studentTheses/caustics-and-catastrophes-in-strong-field-physics/.

[77] E. Delabaere and C. J. Howls, Global asymptotics for multiple integrals with boundaries, Duke Math. J. **112**, 251 (2002).

[78] A. Alexandru, G. Başar, and P. Bedaque, Monte Carlo algorithm for simulating fermions on Lefschetz thimbles, Phys. Rev. D **93**, 014504 (2016).

[79] J. Nishimura and S. Shimasaki, Combining the complex Langevin method and the generalized Lefschetz-thimble method, J. High Energy Phys. 06 (2017) 023.

[80] J. L. Feldbrugge, U.-L. Pen, and N. Turok, Picard–Lefschetz path integrals, GitHub, https://p-lpi.github.io/.

[81] G. E. Bartholomew, Numerical integration over the triangle, Math. Tables Other Aids Comput. **13**, 295 (1959).

[82] M. Han, Z. Huang, H. Liu, *et al.*, Spinfoam on a Lefschetz thimble: Markov chain Monte Carlo computation of a Lorentzian spinfoam propagator, Phys. Rev. D **103**, 084026 (2021).

[83] A. Alexandru, G. Başar, P. F. Bedaque, and N. C. Warrington, Complex paths around the sign problem, Rev. Mod. Phys. **94**, 015006 (2022).

[84] Y. Shoji and K. Trailović, Stable evaluation of Lefschetz thimble intersection numbers: Towards real-time path integrals, Phys. Lett. B **873**, 140198 (2026).

[85] S. K. Lando, Geometry of the Stokes sets for families of functions of one variable, J. Math. Sci. **83**, 534 (1997).

[86] L. E. Chipperfield, L. N. Gaier, P. L. Knight, *et al.*, Conditions for the reliable production of attosecond pulses using ultrashort laser-generated high harmonics, J. Mod. Opt. **52**, 243 (2005).

[87] F. J. Wright, The Stokes set of the cusp diffraction catastrophe, J. Phys. A: Math. Gen. **13**, 2913 (1980).

[88] M. V. Berry and C. J. Howls, Stokes surfaces of diffraction catastrophes with codimension three, Nonlinearity **3**, 281 (1990).

[89] J. Feldbrugge, R. van de Weygaert, J. Hidding, and J. Feldbrugge, Caustic skeleton & cosmic web, J. Cosmol. Astropart. Phys. 05 (2018) 027.

[90] T. Poston and I. Stewart, *Catastrophe Theory and its Applications*, 1st ed., Surveys and Reference Works in Mathematics, Vol. 2 (Pitman Publishing Ltd., Bath, UK, 1978).

[91] P. T. Saunders, *An Introduction to Catastrophe Theory* (Cambridge University Press, Cambridge, 1980).

[92] *NIST Handbook of Mathematical Functions,* edited by F. W. J. Olver, D. W. Lozier, R. F. Boisvert, and C. W. Clark (Cambridge University Press, Cambridge, 2010).

[93] C. Chester, B. Friedman, and F. Ursell, An extension of the method of steepest descents, Math. Proc. Cambridge Philos. Soc. **53**, 599 (1957).

[94] M. V. Berry, Uniform asymptotic smoothing of Stokes's discontinuities, Proc. R. Soc. A. Math. Phys. Sci. **422**, 7 (1989).

[95] H. Schomerus and M. Sieber, Bifurcations of periodic orbits and uniform approximations, J. Phys. A: Math. Gen. **30**, 4537 (1997).

[96] J. J. Stamnes and B. Spjelkavik, Evaluation of the field near a cusp of a caustic, Optica Acta: Int. J. Opt. **30**, 1331 (1983).

[97] L. E. Chipperfield, P. L. Knight, J. W. G. Tisch, and J. P. Marangos, Tracking individual electron trajectories in a high harmonic spectrum, Opt. Commun. **264**, 494 (2006).

[98] O. Pedatzur, G. Orenstein, V. Serbinenko, *et al.*, Attosecond tunnelling interferometry, Nat. Phys. **11**, 815 (2015).

[99] X. Zou, L. Jurkovičová, A. Weber, *et al.*, 2D quantum-path interference in high-harmonic generation driven by highly-bichromatic fields, arXiv:2604.12838.

[100] V. V. Strelkov, M. A. Khokhlova, A. A. Gonoskov, *et al.*, High-order harmonic generation by atoms in an elliptically polarized laser field: Harmonic polarization properties and laser threshold ellipticity, Phys. Rev. A **86**, 013404 (2012).

[101] E. Pisanty and Á. Jiménez-Galán, Strong-field approximation in a rotating frame: High-order harmonic emission from *p* states in bicircular fields, Phys. Rev. A **96**, 063401 (2017).

[102] E. Pisanty, D. D. Hickstein, B. R. Galloway, *et al.*, High harmonic interferometry of the Lorentz force in strong mid-infrared laser fields, New J. Phys. **20**, 053036 (2018).

[103] J. Itatani, J. Levesque, D. Zeidler, *et al.*, Tomographic imaging of molecular orbitals, Nature (London) **432**, 867 (2004).

[104] A. Zaïr, M. Holler, A. Guandalini, *et al.*, Quantum path interferences in high-order harmonic generation, Phys. Rev. Lett. **100**, 143902 (2008).

[105] D. J. Hoffmann, C. Hutchison, A. Zaïr, and J. P. Marangos, Control of temporal mapping and harmonic intensity modulation using two-color orthogonally polarized fields, Phys. Rev. A **89**, 023423 (2014).

[106] L. Brugnera, D. J. Hoffmann, T. Siegel, *et al.*, Trajectory selection in high harmonic generation by controlling the phase between orthogonal two-color fields, Phys. Rev. Lett. **107**, 153902 (2011).

[107] T.-M. Yan, S. V. Popruzhenko, M. J. J. Vrakking, and D. Bauer, Low-energy structures in strong field ionization revealed by quantum orbits, Phys. Rev. Lett. **105**, 253002 (2010).

[108] A. J. Uzan, G. Orenstein, Á. Jiménez-Galán, *et al.*, Attosecond spectral singularities in solid-state high-harmonic generation, Nat. Photon. **14**, 183 (2020).

[109] S. P. Goreslavskii and S. V. Popruzhenko, Tunneling limit in the theory of photoelectron rescattering by the parent ion, J. Exp. Theor. Phys. **90**, 778 (2000).

[110] T. Rook and C. Figueira De Morisson Faria, Exploring symmetries in photoelectron holography with two-color linearly polarized fields, J. Phys. B: At. Mol. Opt. Phys. **55**, 165601 (2022).

[111] D. Habibović, W. Becker, and D. B. Milošević, Complete classification and additional saddle-point solutions for high-order above-threshold ionization induced by a strong laser field. II. Classical considerations, Phys. Rev. A **111**, 053110 (2025).

[112] M. V. Berry, Focusing and twinkling: Critical exponents from catastrophes in non-Gaussian random short waves, J. Phys. A: Math. Gen. **10**, 2061 (1977).

[113] M. V. Berry and C. J. Howls, Hyperasymptotics for integrals with saddles, Proc. R. Soc. Lond. Ser. A **434**, 657 (1991).

[114] D. Dorigoni, An introduction to resurgence, trans-series and alien calculus, Ann. Phys. **409**, 167914 (2019).

[115] P. V. Demekhin and L. S. Cederbaum, Dynamic interference of photoelectrons produced by high-frequency laser pulses, Phys. Rev. Lett. **108**, 253001 (2012).

[116] F. Vismarra, M. Bertolino, E. Appi, *et al.*, Dynamic interference of chirped photoelectrons, Phys. Rev. Lett. **135**, 033202 (2025).

[117] J. Itatani, F. Quéré, G. L. Yudin, *et al.*, Attosecond streak camera, Phys. Rev. Lett. **88**, 173903 (2002).

[118] D. Moos, H. Jürß, and D. Bauer, Intense-laser-driven electron dynamics and high-order harmonic generation in solids including topological effects, Phys. Rev. A **102**, 053112 (2020).